 doi:10.20944/preprints202209.0070.v1

Density and velocity analysis of the planetary nebula NGC 6853

Robert Hrubý[1]

[1] *Faculty of Nuclear Sciences and Physical Engineering, Czech Technical University in Prague, Břehová 7, Prague, 110 00, Czech Republic*

September 8, 2022

Abstract

In stellar NGC 6853, also known as the Dumbbell Nebula, It is a remarkable example of an elliptical morphological type 1 multiple shell planetary nebula, which is now in one of its last evolutionary stages. This project focuses on examining the distinct varieties of the nebula temperatures and densities using observation data from the Issac Newton Group of Telescopes and comparing them with the observation data from Observatoire de Haute Provence from 14th till 18th of October 2019, with a primary focus on the data from the Issac Newton Telescope (INT). The densities ranged from diffused regions of 376.63 ± 228.97 atoms per cm^3 to dense regions of 6441.11 ± 228.90 atoms per cm^3; these values are slightly lower approximately by 2000 than the values from the Observatoire de Haute Provence. The radial velocity and the expansion velocity were also calculated using the spectroscopic data and was found to be 29.50 ± 0.38 km^{-1} and 37.40 ± 0.38 km^{-1} respectively. This result is expected from a multi-shell nebula that consists of a main body and surrounding halo.

Keywords— Nebula, NGC-6853, Stellar, Deep space, Remnant, analysis, Dumbbell nebula

 doi:10.20944/preprints202209.0070.v1

Declaration of Authorship

I have read and understood the departmental policy on plagiarism. I declare that this thesis is my own work and has not been submitted in any form for another degree or diploma at any university or other institution of tertiary education. Information derived from the published or unpublished work of others has been acknowledged in the text and a list of references is given.

Robert Hrubý
September 8, 2022

 doi:10.20944/preprints202209.0070.v1

Acknowledgements

I would like to thank Dr. Emma Whelan, Dr. Créidhe O'Sullivan, Dr. Patrick Kavanagh, for their advice throughout the course of my research project. I'd also like to thank Darren Cashin for his advice.

I am unbelievably indebted to Matthew Birney for working with me in taking measurements at the Observatoire de Haute-Provence and providing his constant support and cooperation during the data analysis.

I would also like to thank Tristan, Michael, Sarah and Courtney for helping me stay motivated and keep going through the long nights in the laboratory and through the pandemic crisis on Messenger as a group.

Last but not the least, I would like to thank my mom and my family and Patricia and my friends for their continued support throughout my degree.

List of Figures

 doi:10.20944/preprints202209.0070.v1

List of Tables

 doi:10.20944/preprints202209.0070.v1

Contents

1 Introduction

"Planetary nebulae are a visually spectacular and relatively short-lived step in the evolution from asymptotic giant branch (AGB) stars, to a final white dwarf stage" (G. Benedict et al. 2007).

As nebulae are shells of gas and dust that are ejected from a star at an extensive range of the electromagnetic spectrum, from radio to gamma rays, this phenomenon is done by the "process of its evolution from a hydrogen-burning main sequence star into a red giant and eventually into a white dwarf." However, the process described above does not happen to every star; this occurs only for stars with an initial mass of $0.8M0 < M < 6M0$. These interstellar objects have a relatively short lifespan, which is in the order of 20 000 years, making them moderately rare (*Planetary Nebulae | www.cfa.harvard.edu/* 2020).

The HII emission line is the line in spectra that allowed the first observation of planetary nebulae by Charles Messier in 1764 and was given the number 27 in his catalog. William Huggins then took the first spectrum of a planetary nebula in 1864. Since the luminosity is not due to the reflection of incoming starlight, the spectra of a planetary nebula are completely different from its centra stars. Due to the rapid mass loss which exposes the stellar core, the radiation from the core ionizes the gas resulting in a planetary nebula (Kwok 2007).

It is possible to determine the elements present in gaseous nebulas by looking at the spectra lines. The first excited state of a hydrogen atom is 10.20 eV above the ground state, which can be corresponded to an ideal excitation temperature of 12^5K. That is hotter than the standard temperature of a planetary nebula, which is $\approx 10^4K$ (Seaton 1954).

Planetary nebulae play a very significant role in the evolution of the galactic plane as a star that goes through all of its primary sequences. The fusion reaction, which is taking place in the core of the star, produces heavier elements as time goes on. This system causes the nebula to contain many heavy elements. Even when these elements did not exist at first in the early universe, they got diffused into the interstellar medium through the system. The new and younger stars that are formed then contain higher metal content, eventually allowing the evolution of the universe (Kwok 2007).

 doi:10.20944/preprints202209.0070.v1

2 Origin of Planetary Nebulae

Nothing lasts forever, and thus, a medium-size star typically evolves into planetary nebulae.

Phase one is where all hydrogen in the star fuses into helium through proton-proton chain. Proton-proton chain works on the base that four hydrogen atoms fuse to form one helium nucleus. When the star runs out of hydrogen to fuse (burn), then phase two occurs. Here, as the core collapses, the pressure and temperature increase, and the helium begins to fuse into heavier elements such as carbon and oxygen, eventually iron. This procedure produces a tremendous amount of radiation from within, causing the pressure which pushes back on gravity to increase. Eventually, gravity will balance this pressure; however, that is, after the star becomes multiple times its original size and thus colder; hence it will appear red, and this marks the beginning of the red giant phase.

Phase three is the phase where the the amount of helium in the star's core becomes exhausted as it did with hydrogen in phase one, and the gravity will cause the star to shrink suddenly. When the thermonuclear reaction within the shell of helium commences, the outward radiation pressure will exceed the gravity, causing the surface to return to its original red giant state with a small difference. The force of gravity will be insufficient to stop the expansion. Hence, the outer portion of the star will separate and drift away from the central region containing the core of the star. Once the star has shredded, the majority of its shells, particles, and gasses will begin to visibly glow in "harlequin colors" (*Formation of Planetary Nebulae* 2020) as it is ionized by many high energized particles of the electromagnetic spectrum coming from the hot core.

As the surface materials depart, the core will be visible. Inside this core is a very dense and small star called a white dwarf. A White dwarf is a class of star that has approximately the mass of sun contained in a volume of earth (Shapiro and Teukolsky 2008).

It takes approximately 15,000 - 20,000 years for planetary nebulae to fade into obscurity, in which the material of the nebula becomes an essential part of the interstellar medium (ISM). This material are fundamental for the recycling of hydrogen and also react as an agent that introduces new elements into the interstellar medium (ISM) such as carbon, oxygen, nitrogen, and other elements that are vital for existence (Griffiths 2012).

Preprints (www.preprints.org) | NOT PEER-REVIEWED | Posted: 5 September 2022 doi:10.20944/preprints202209.0070.v1

2.1 NGC 6853

The Dumbbell nebula (NGC 6853) is the large nearby planetary nebula located in the constellation Vulpecula. It is to be around 1,200 light-years from earth [$\alpha = 19^h\ 59^m\ 36.363^s$, $\delta = +22°\ 43'\ 16.31"$]. (G. F. Benedict et al. 2003)

NGC 6853 nebula is often referred as the Messier 27 which is the name given by Charles Messier, the famous French comet hunter who noticed its distant, faint fuzzy circular glow and placed it in his catalog. A few years later, the musician turned astronomer named William Herschel gave these objects their name because they resemble planets. Resulting in the Dumbbell nebula to be the first ever observed/discovered planetary nebula (*Formation of Planetary Nebulae* 2020).

Despite its class, the Dumbbell Nebula has nothing to do with planets. Within its core is a star that is classified white dwarf, with a visual magnitude V = 13.98 ± 0.03, and absolute magnitude Mv = 5.43 ± 0.3. The radii of the white dwarf was calculated to be R = 0.055 ± 0.02 $R_\odot$ by (Napiwotzki 1999), together with its mass M = 0.56 ± 0.01 $M_\odot$ by (G. Benedict et al. 2007). These parameters make the central star of NGC 6853 the largest white dwarf that is known.

The effective temperature of the center star is $T_{eff} \approx$ between 100,000 K and 108,600 K, with the excitation class to be calculated p = 10. This excitation is to be considered a high excitation class see Figure 3.2 or 3.3. The excitation tells that the planetary nebula must have hot and very hot nuclei, which means a high ionization of the dust and gas around the nebula is to be expected, giving its glow and temperature (Gurzadyan 2013).

 doi:10.20944/preprints202209.0070.v1

Figure 2.1: This image was produced with a RCOS half meter telescope and Astrodon E-Series filters. H-alpha, OIII (All 1X1). Image copyright ©2011 (R Jay GaBany) (*The Dumbbell Nebula (NGC 6853, M27)* 2020)

Figure 2.2: All the images are in this orientation

3 Theory

3.1 Spectral lines in Planetary Nebulae

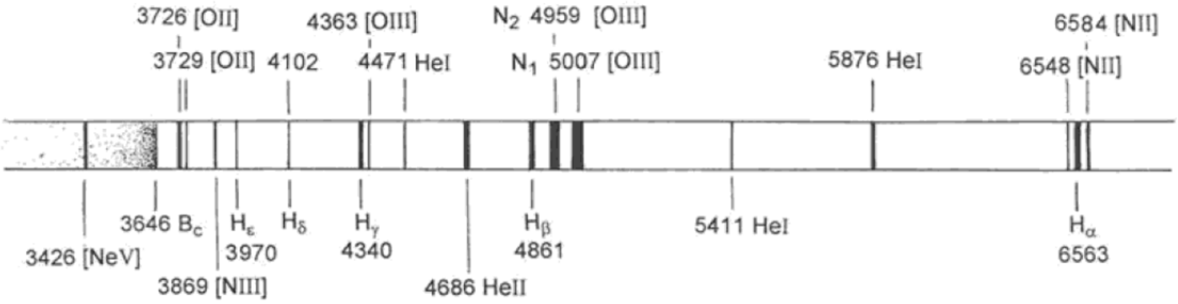

Figure 3.1: General structure of the spectrum of a planetary nebula in the optical region (Gurzadyan 2013)

The spectrum of planetary nebulae for an optical region consists of a series of intense and weak emission lines. This is in stark contrast to a star, which is a continuous spectrum. These line emissions occur when atoms undergo transmission from one energy state to another lower energy state. Consider electron transitions withing a hydrogen atom for energy state n $= 3 \rightarrow 2$. This gives rise to H_α while n $= 4 \rightarrow 2$ gives rise to H_β. Wavelengths that correspond to the emissions lines in Figure 3.1 are given by equation 3.1 (Gurzadyan 2013).

$$\frac{1}{\lambda} = R(\frac{1}{2^2} - \frac{1}{n^2}) \tag{3.1}$$

Where λ is the wavelength and R is the Rydberg constant (1.097 x 10^7 m^{-1}).

The only way an excited electron bounded by an atom can be found, is then by collisional excitation from lower state or as a result of recombination (Kwok 2007). Since hydrogen atoms cannot be exited by collisions due to nebula's relatively low density, hence, it is vital to have other accurate means of measure. Such as the estimate of electron density N_e and electron temperature T_e which can be reliably obtained from a relating of the emission intensities of H_α and H_β, this ratio is called Balmer Intensity, for which a theoretical Balmer Intensity for nebula at 10^4 K exist and is equal to 2.86 (Hummer and Storey 1987).

Preprints (www.preprints.org) | NOT PEER-REVIEWED | Posted: 5 September 2022 doi:10.20944/preprints202209.0070.v1

The excitation class of a nebula p is a measurement of the collisional excitation. An integer number indicates it from 1 up to 12+, and the whole sequence of planetary nebulae is divided into three groups, which are according to the degree of excitation. For low excitation planetary nebula, the nuclei should be of low temperature. On the other hand, if the case is of high excitation, then the planetary nebula must have hot and very hot nuclei. For which the concept of excitation appeared and has a classification, see Figure 3.2 and 3.3 (Gurzadyan 2013).

p	$\frac{N_1+N_2}{H_\beta}$	p	$\log\frac{N_1+N_2}{4686}$	p	$\log\frac{N_1+N_2}{4686}$
	Low		Middle		High
1	0– 5	4	2.6	9	1.7
2	5–10	5	2.5	10	1.5
3	10–15	6	2.3	11	1.2
4	>15	7	2.1	12	0.9
		8	1.9	12^+	0.6

Figure 3.2: Excitation class p of planetary nebula (Gurzadyan 2013)

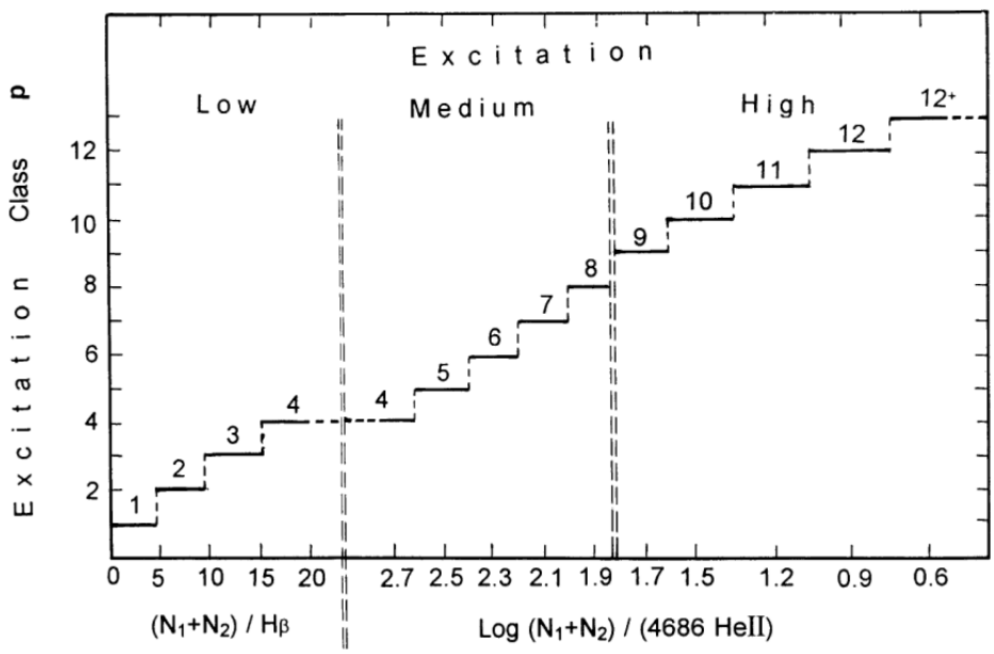

Figure 3.3: Graphical representation of excitation class p, of gaseous nebulae (Gurzadyan 2013)

 doi:10.20944/preprints202209.0070.v1

3.2 Forbidden Lines

Hydrogen is the most abundant element in the nebula. However, the radiated energy from heavier elements is higher than that of hydrogen. This is due to the efficiency causing to offset the higher abundances hydrogen. Since the central star is continuously illuminating the gas around, this would cause the temperature to increase infinitely if there are no cooling mechanisms. However, it is known that the temperature is in the order 10^4 K, from Balmer Intensity.

The cooling mechanism also called a forbidden mechanism or forbidden lines, is a concept in physics where a spectra line emitted by atoms is undergoing energy transitions that are not normally allowed by the selection rule of quantum mechanics. This means that the process cannot undergo its most efficient (electrical dipole) route. Although the transition is normally "forbidden", there is a non-zero probability of their spontaneous occurrence. These emission lines have only been observed in extremely low-density gasses in outer space. Nebular cloud has these lines which are extremely important for cooling; they are denoted in square brackets and the mechanisms which produce the transitions corresponding to O^+ [OII] and O^{2+} [OIII] lines. See Table 3.1 for transitions (Sindhu 2006), (Draine 2010).

Parity	Must change
ΔL	0, ± 1
ΔJ	0, ± 1 however J = 0 → 0 is forbidden
Δl	± 1
ΔS	± 0 Spin does not change

Table 3.1: Selection rule for electric dipole transitions (Draine 2010)

Forbidden line is one that fails to satisfy one of the first four selection rules presented in Table 3.1. Forbidden lines are quite particular in astronomical processes due to the low densities. Planetary nebulae densities range from 100 to 10,000 particles cm^{-3} (Donald E Osterbrock and Ferland 2006). The [OIII] doublet can be seen in Figure 3.1. Since the density in the nebula is low, the collisions are rare, explaining that the only decay path is via forbidden lines since there is a sufficient amount of time (Draine 2010).

Preprints (www.preprints.org) | NOT PEER-REVIEWED | Posted: 5 September 2022 doi:10.20944/preprints202209.0070.v1

4 Instrumentation

4.1 Coordinate System

In astronomy, various coordinate systems are used to determine the position of an astronomical object in the sky. The most well known coordinate system that is primary uses is a "celestial sphere." Think of an imaginary sphere of infinite radius enveloping the earth inside this sphere. Onto the surface of this envelope, all astronomical objects are projected. The celestial sphere does not change orientation. However, as the earth rotates (west to east), the celestial sphere also appears to rotate in the opposite direction.

4.1.1 Alt-Azimuth

Alt/az (Altitude and azimuth) local system that describes the sky for one observer at one location means that it is dependent on the observation longitude and latitude. The Alt-Azimuth system used the observer's local horizon as a reference. The altitude (Alt) is the angular distance measured above the local horizon to the desired object, and it ranges from $0°$ to $90°$, where $90°$ is called the zenith, which is directly above the observer. Azimuth is the angular distance measured from true north on its horizon (Alt $= 0$). The starting value for azimuth is $0°$, that would be the direction of true north, as the angle propagate it increases eastwards, east azimuth is $90°$, and so on. The range of azimuth is from $0°$ to $360°$. The major negative aspect of the Alt-azimuth system is that it is not a global coordinate system; observers from or at different locations on Earth will not agree on the position of an object in the sky. Alt-Azimuth. The Alt-Azimuth system can be viewed in Figure 4.1.

4.1.2 Equatorial coordinate system

The RA/Dec celestial coordinates are used to pinpoint the position of the desired object on the celestial sphere. The earth is split into two hemispheres. This is then divided by a circle that surrounds the equator of the earth. This line is called the celestial equator, where the north celestial pole is directly above the north pole, and this is also true for the south celestial pole. The abbreviated declination (Dec), is the coordinate between these two poles. It is measured from the celestial equator where the declination is $0°$ going to $\pm 90°$ for North/South poles respectively.

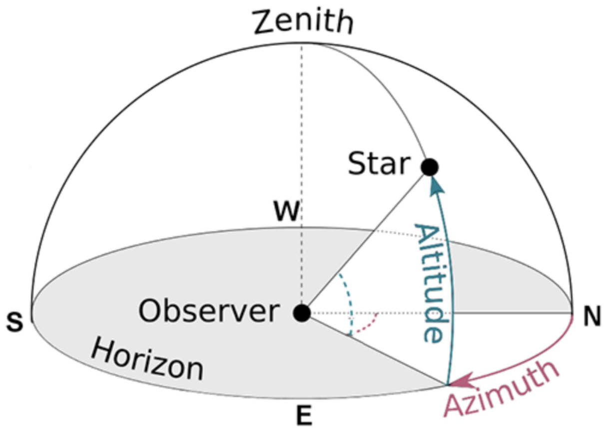

Figure 4.1: Alt-Azimuth co-ordinate system (University 2020)

Right Ascension abbreviated RA, is the second coordinate in the celestial equatorial system. It is the angular distance of a particular point, measured in hours, minutes, and seconds eastwards along the celestial equator (great circle of the imaginary celestial sphere) from the sun at the vernal equinox. Taking the rotation of the earth into consideration, the Right Ascension is divided into 24 hours. The celestial equatorial system can be viewed in Figure 4.2.

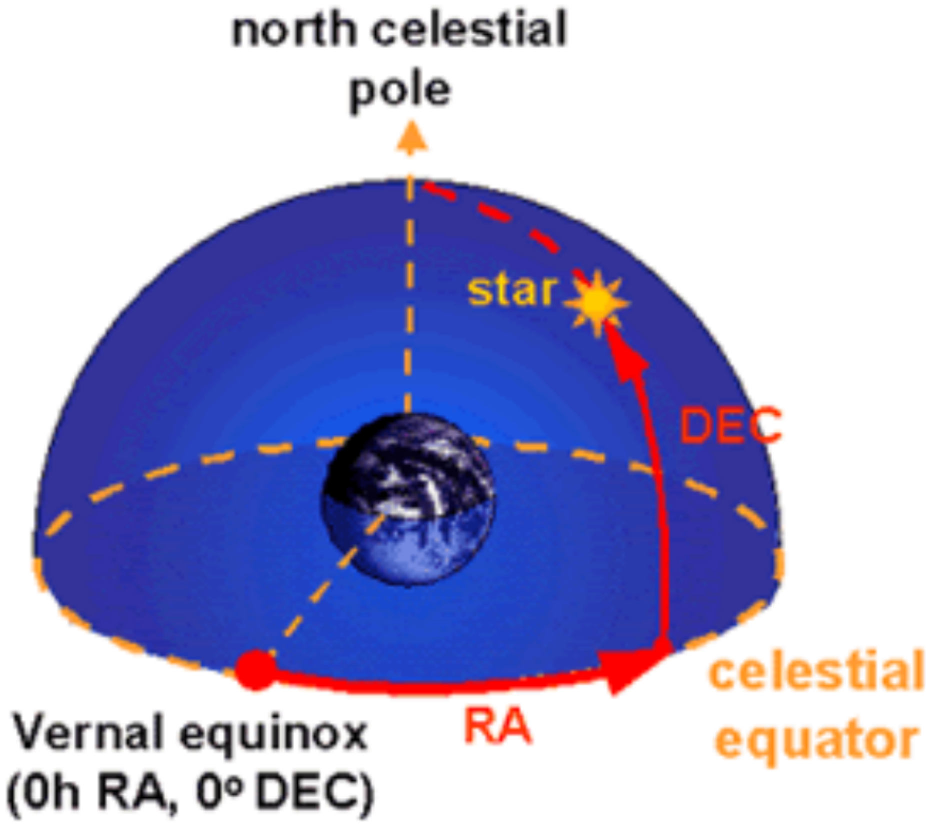

Figure 4.2: RA-Declination (*Swinburne University / Melbourne, Australia* 2020)

4.2 Charge-Coupled Devices

A charge-coupled device (CCD) is an array of solid-state detectors on a single silicon chip. In each chip, there is approximately 10^7 pixels. The incoming photons which are collected via telescope are introduced onto the semiconductor which produces a charge distribution over the array. The accumulated charge is read out by transferring it along a line of directors to record as is it reaches the end of the line, hence the name Charge-Coupled Devices. The CCDs move charge between capacitive bins in the device, with the shift allowing for the transfer of charge between bins. The electrons accrue on capacitors until their number is read out by the CCD after the integration time. This number is proportional to the light intensity at the location. The p-type silicon substrate is at positive voltage to the electrode, the p-n junction is reverse biased, depending on the potential well in the n-type silicone directly below the electrode. Incident light generates electron-hole pairs, which then migrate upwards into the n-type silicone where they are trapped.

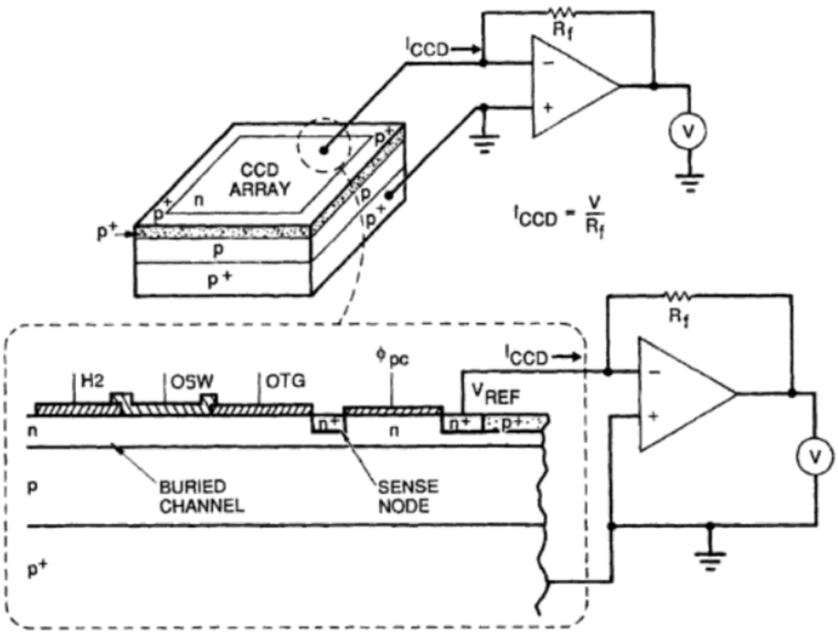

Figure 4.3: CCD cell (Janesick 2001)

CCDs are popular in astronomy due to a dynamic range that is $\approx 10^6$ - 1, high quantum efficiency, and from the ease with which arrays can be used for two-dimensional imaging, low read-out noise, and broad spectra response (400-1000 nm). Couple disadvantages such as performance sensitivity to chip defects, sensitivity varying across the chip, results in the most necessary need for flat filed. Due to the size of pixels that are of $microns^2$, the resolution is lowered. Most of

 doi:10.20944/preprints202209.0070.v1

the original limitations of the CCDs have now been overcome and have led to a large format CCD detector today. Nowadays, the CCDs detector is cryogenically cooled to reduce the temperature, which would give energy to the electrons that are not produced by incident photons resulting in increase of dark current.

4.3 La Palma of the Canary Islands

4.3.1 The 254 cm Isaac Newton Telescope (INT)

The Isaac Newton Telescope (INT) is a cassegrain telescope with a primary diameter of 254 cm and a focal lenght of 8.36m. The focal ratio is f/3.29 with a mounting that is a polar disc/fork type equatorial mounting, this gives rotation limitations as follow: Zenith distance $< 70°$, - 6 h $<$ hour angle $< +$ 6 h (above pole), Declination $> -30° \ 09' \ 30"$.

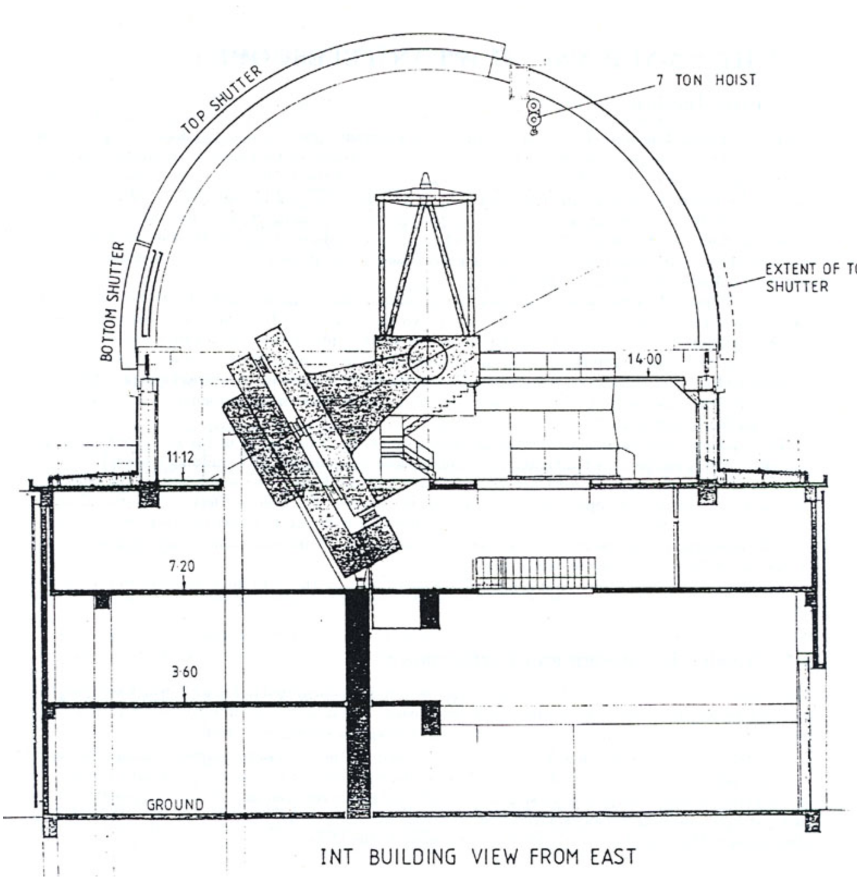

Figure 4.4: The Isaac Newton Telescope Schematic Diagram. Credit:(RGO 2020)

Cassegrain is a reflecting telescope that uses a primary paraboloidal mirror with a hyperboloidal secondary. Since Cassegrain relies on reflection, that means it is free of chromatic aberrations, but due to the paraboloidal mirror, it suffers from coma and off-axis astigmatism. The camera of the 254 cm is an optical mosaic camera, a wide field camera (WFC). Optimized for the visible wavelengths (500 nm - 650 nm) there is a quantum yield of more than 95% in this range. The WFC consists of 4 thinned EEV 2048 X 4100 CCDs. The CCDs have a pixel size of 13.5 microns corresponding to 0.33 arcsec/pixel. A maximum of 6 filters could be installed in the wheel (Isac Newton Group of Telescopes 2020).

4.4 Haute-Provence France

4.4.1 152 cm Telescope

The 152 cm telescope contains only a Coude focus, which is a a focal point in an equatorially mounted telescope that lies along the polar axis. “Coude is French for ‘elbow’, referring to the bending of the light path through 90° ” (Ridpath 2012), to focus the light on the detector the mirror of the chamber is moved using the control software. It has (f/30) and uses the Aurelie spectrograph which has dimension range of 2049 x 1024 pixels due to its thin back-illuminated EEV 42-20 CCD chip that allows it to obtain very high resolution spectra. These CCD are sensitive between pixels 46 and 2093 on each line.

Unlike the 254 cm (INT), the 152 cm telescope is used to measure the interstellar lines of NGC 6853’s nebular cloud (spectra). The quantum yield of Aurelie ranges from 50.4% at 350 nm to 33.0% at 900 nm, with the CCD’s having an operating temperature of 163 K (Gillet et al. 1994).

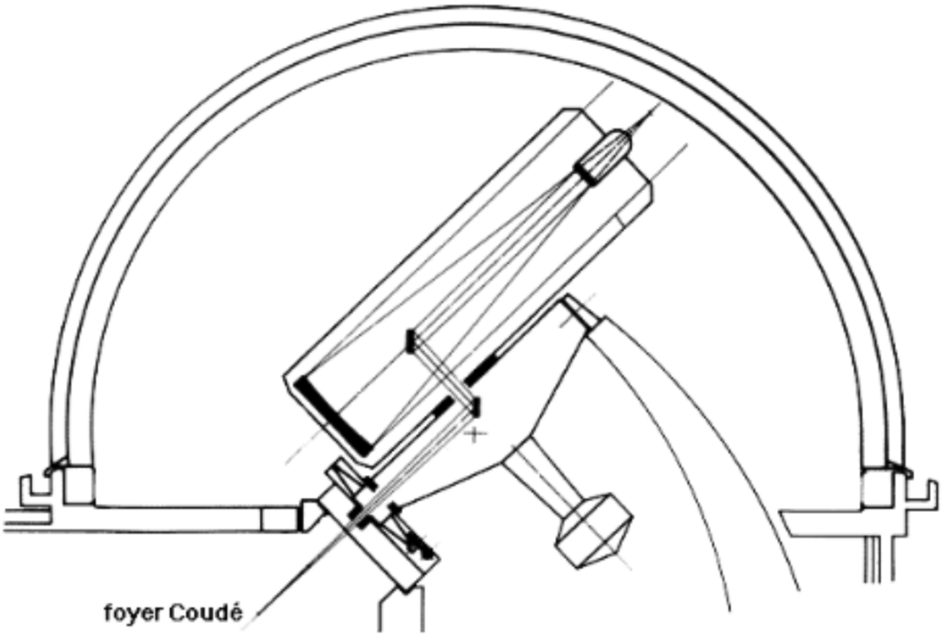

Figure 4.5: The 152 cm OHP Telescope Schematic Diagram (*Tlescope de 1m52 OHP* n.d.)

5 Observation data

5.1 Observational Periods

The aim of this research project was to collect Ha_{α} and H_{β} emissions of NGC 6853 from two different places, the OHP Observatory in France and the Roque de los Muchachos Observatory in La Palma, Spain.

The following Figures 5.1 and 5.2 were obtained from StarAlt which were then used to find and plan the altitude of the celestial object for each night. The mentioned StarAlt website, represents the observatory's conditions on a certain date and time to observe the NGC 6853 nebula.

There are a couple of factors that had to be taken into consideration. The first one is the object altitude on the sky, which is indicated by the y-axis. To collect as much data as possible and to reduce atmospheric distortion, it is suggested not to go bellow 40° as then too much of an atmosphere is in the way. It is visible for both cases that the observation should take time from 20:00 - 23:00.

Next factor that has to be considered is the sunset and sunrise; for which the times corresponded approximately 19:30 - 5 and 20:00 - 6 for OHP and La Palma respectively. See dotted line in Figure 5.1 and 5.2.

Another factor was the angle of the object from the moon. It is indicated by

 doi:10.20944/preprints202209.0070.v1

the blue numbers on the curve. Last but not the least factor is the weather. Both observations have a good geographical location, allowing them to have very favorable observing conditions, on average for OHP is a 60% of nights that are suitable for astronomical observations (*Observatoire de Haute-Provence (OHP)* 2020), and 75% of nights are clear for Roque de Los Muchachos Observatory (Isac Newton Group of Telescopes 2020). The ideal measurements are taken with high altitude and angle from the moon. Find the complete observation log in Appendix A.1

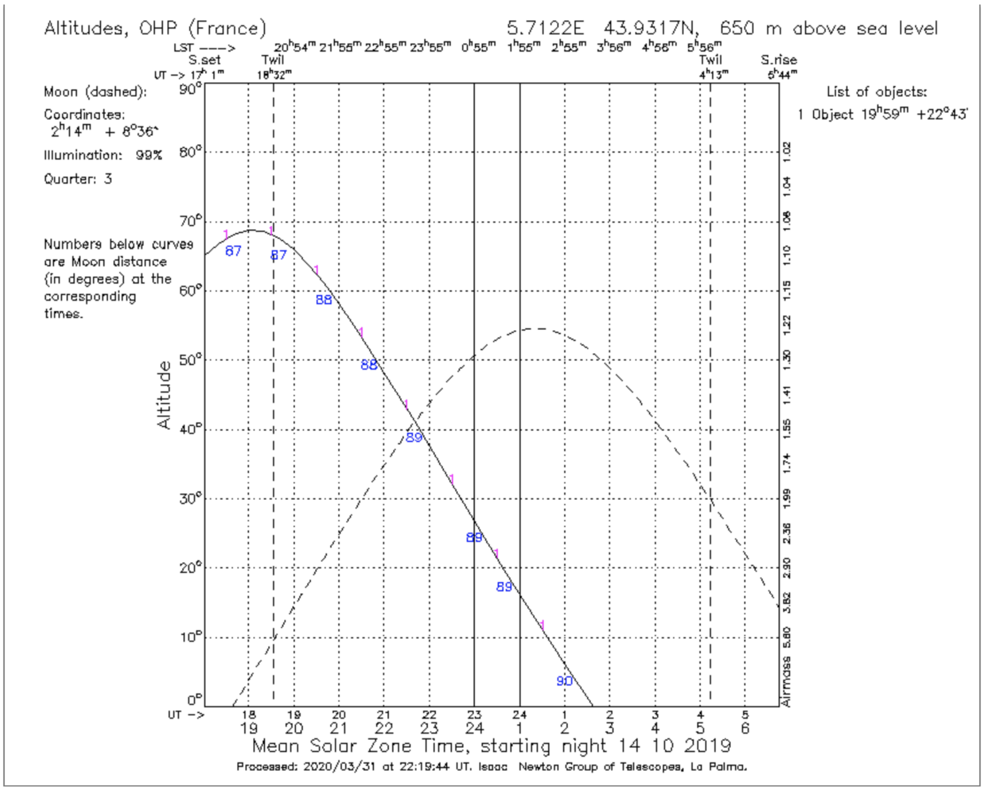

Figure 5.1: NGC 6853 position in the sky throughout the day, OHP

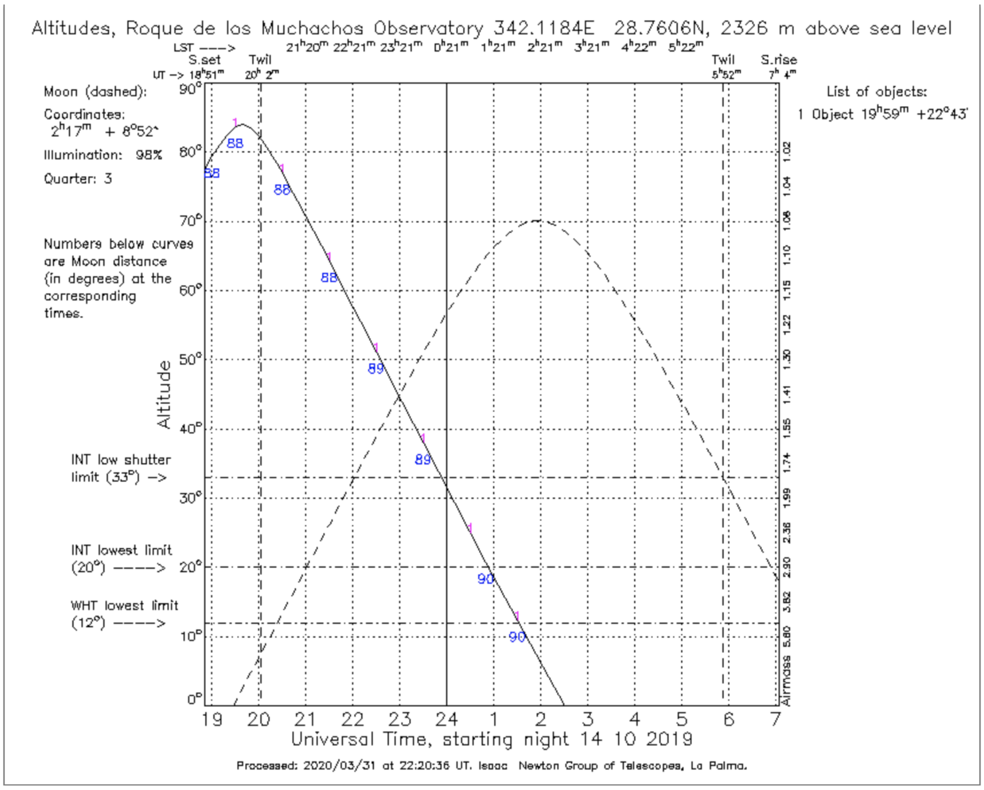

Figure 5.2: NGC 6853 position in the sky throughout the day, Roque de los Muchachos

6 Data Reduction

Data reduction was carried out using IRAF (Image Reduction and Analysis Facility), a command-line based application that is freely available software developed by the National Optical Astronomy Observatory. Python-based astronomical applications called Astropy is slowly taking over; however, IRAF is still more than capable for its purpose. IRAF was used together with the SAOimageDS9 viewer, which allows displaying of .FITS files.

6.1 Purpose of Data Reductions

It is to reduce noise that is caused by cosmic rays, dark current, and other factors, these calibration files and their importance are described in the following subsections.

6.1.1 Darks

Darks are used to account for the pixels on the CCD, which are reading signals generated due to thermal agitation of atoms in the CCD, this is effectively noise that is causing the temperature to not be uniform across the entire array. The darks were taken by keeping the shutter closed during an exposure to ensure no light gets in (Howell 2006).

In the case for the 254 cm (INT) the darks were already taken away from the images, this was checked by looking at the uniform bias image.

6.1.2 Flats

Flat fields are used to correct for the fact that each pixel has a slightly different gain or QE value when compared with its neighbors. In order to flatten the relative response for each pixel to the incoming radiation, a flat field image is obtained and used to perform this calibration. Ideally, a flat field image would consist of uniform illumination of every pixel by a light source of identical spectra response to that of your object frames. That is, you want the flat field image to be spectrally and spatially flat. Once the flat field image is obtained, one then divides each object frame by it, and that results in the instant removal of pixel to pixel variation (Marquez 2012).

6.1.3 Biases

It is a low-level electrical signal added in each pixel when turned on. This is independent of CCD temperature or exposure time. Therefore, a bias is used to account for random noise and is subtracted. Bias frame was taken with a zero-length exposure and with the shutter of the telescope closed (Howell 2006).

6.2 254 cm Telescope Data

The data reduction for the 254 cm telescope was carried out in stages; master flat, master bias, and the raw image, there was no need for master dark as the dark was already subtracted. When these masters were created minus the dark, the following formula which is modified from the original resulted in achieving the final image:

$$Final\ Image = \frac{Raw\ Image - Master\ Bias}{Master\ Flat - Master\ Bias} \tag{6.1}$$

To get the master images, which are combinations of many sub-images aligned correctly, the *imcombine* task in IRAF was used. An example of how the master bias and master flat was made can be seen respectively below. This was carried out in both H_α and H_β.

cl> imcombine @Biaslist Master_Bias.fits combine=median

 doi:10.20944/preprints202209.0070.v1

cl> imcombine @Flats Masterflat.fits combine=median

cl> imarith Masterflat.fits - Master_Bias.fits Master_flat_bias.fits

These master images then had to be normalized. That was done by using the images own mode (average value) which was divided into the master image. To obtain the mode package *imstat* was used, this then followed using package *imarith* to divide the master images by the mode.

H_α images were combined using the *imcombine* command. All the H_α images were named in a list called Ha_ list. When these images were combined, the *imarith* command was used to to carry out the equations 6.1. This was carried out again for H_β using a similar method.

cl> imcombine @Ha_list Ha_composite.fits combine=median

cl> imarith Ha_composite.fits - Master_Bias.fits Ha_bias.fits

cl> imarith Ha_bias.fits / Master_flat_bias.fits Ha_FINAL.fits

Final image for master bias can be seen in Figure 6.1, and master flat for both H_α and H_β in Figure 6.2.

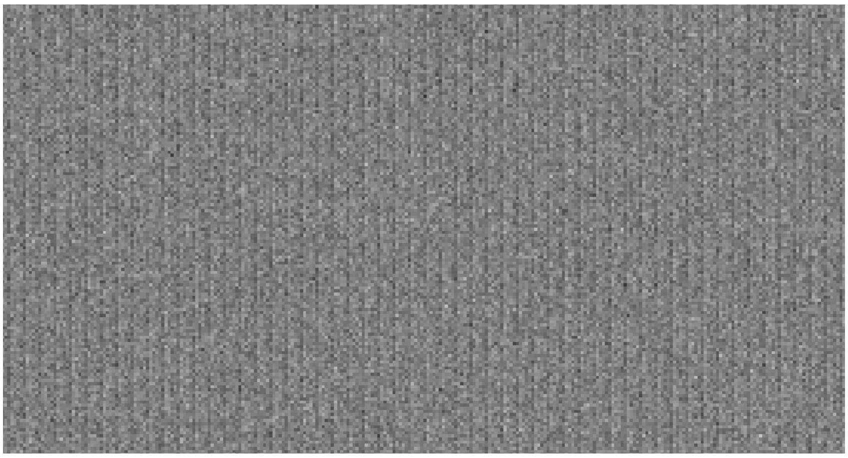

Figure 6.1: The master bias for the 254 cm

Due to the movement of the nebula, it was necessary to align the images using the *imalign* command. This is done by taking a guide star and aligning them on top of each other. At first, the *imalign* worked for the H_α and OIII. However, it did not recognize the H_β guide stars. This was caused because the whole array of pixels for H_β did not start from 0 but instead from - 50. Hence, the aperture was not in range. Even if manual image shifts *imshift* was introduced, it still did not shift the star far enough where it should. After correcting for the -50 starting point through *hedit*, then the *imalign* tool worked for all three images, H_α, H_β and OIII. An example of how imalign was attempted can be seen on next page.

Preprints (www.preprints.org) | NOT PEER-REVIEWED | Posted: 5 September 2022 doi:10.20944/preprints202209.0070.v1

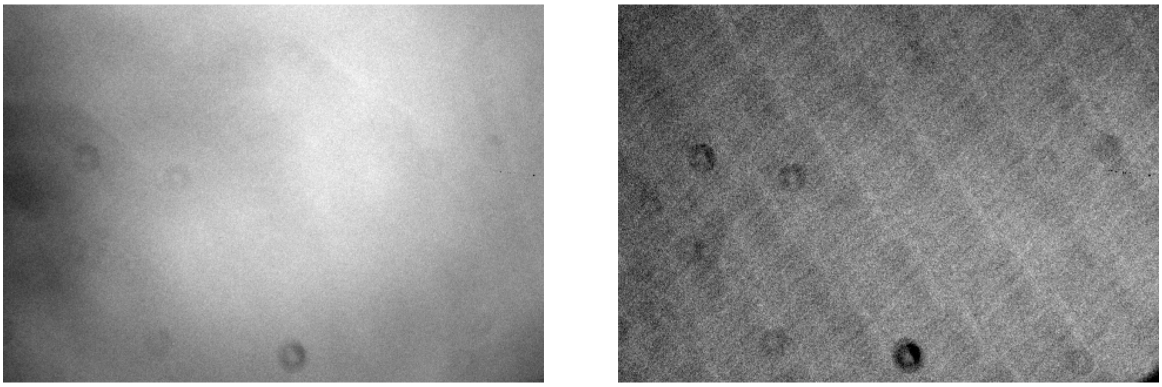

Figure 6.2: The master flats for H_α (left) and H_β (right) for the 254 cm.

cl> imalign @NGC_list H_α FINAL.fits star.txt NGC_list

First, a list that contained H_α_FINAL.fits, H_β_FINAL.fits, OIII_FINAL.fits was created, then a .txt file that contained coordinates of guide stars that were picked from H_α_FINAL.fits. This will cause the other two images to align with the H_α_FINAL.fits image and replaces the original. The final aligned images for H_α, H_β, OIII can be seen in Figure 6.3, Figure 6.4 and Figure 6.5 respectively. Note that the OIII is used only for its spectrum, which falls in the green color. This allowed the usage of RGB to obtain the full color range of this nebula. By looking at the three figures, we can already see different structures and variations between different areas in the nebula.

cl> ds9 rgb - red HaF.fits - blue HbF.fits - green OIIIF.fits

Where HaF.fits represent H_α_FINAL.fits, HbF,fits represent H_β_FINAL.fits and OIIIF.fits represent OIII_FINAL.fits. The pixel levels were edited in IRAF. This produced the nebula's "true" color image, which can be seen in Figure 6.6. This true-color image shows the different variations in the levels of H_α, H_β and as an extra filter the OIII, in a clearer perspective than its greyscale version. However, note this probably is not the nebula's true color, this image or the idea of this color, they are all theoretical assumptions from the knowledge that each spectrum at some wavelength reproduces some specific color. So it is more likely that the actual color reproduced, however, is not a direct observation of color. In a way it is just an adding color to filter and overlapping them.

Another way of representing the final "true" color image with much higher quality and detail was done in Adobe Photoshop. This was done in combination with Liberator 3, which is a software developed in collaboration with ESA, ESO, and NASA. It allows astronomers and the more targeted group astrophotographers a conversion of .FITS files into a format that Adobe Photoshop is more

 doi:10.20944/preprints202209.0070.v1

familiar with, such as .TIFF format. The “true colour” image can be then seen in Figure 6.7.

Preprints (www.preprints.org) | NOT PEER-REVIEWED | Posted: 5 September 2022 doi:10.20944/preprints202209.0070.v1

Figure 6.3: Final aligned H_α image

Figure 6.4: Final aligned H_β image

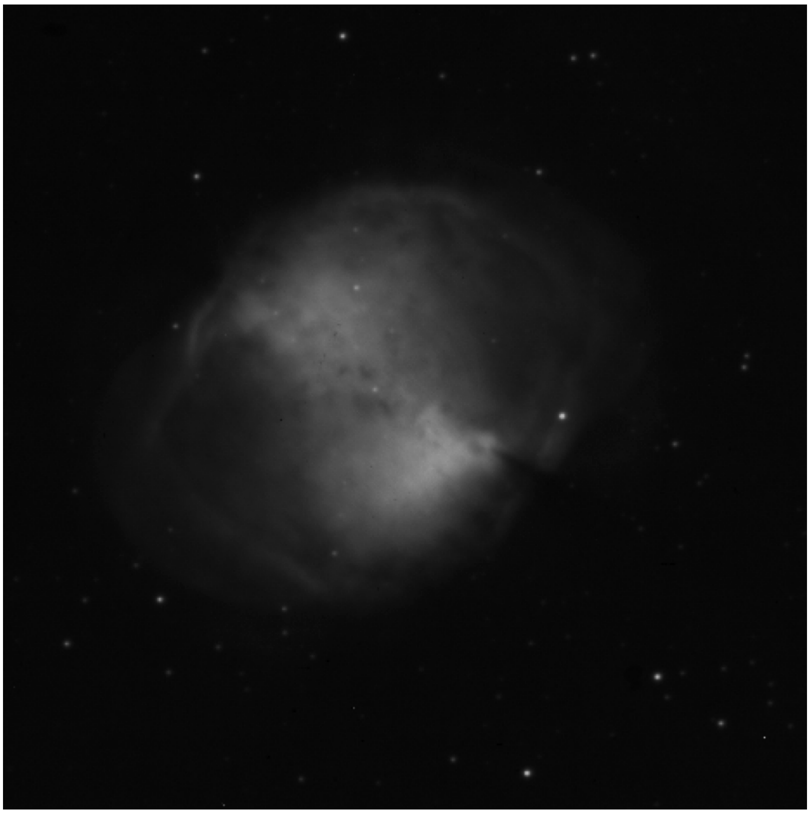

Figure 6.5: Final aligned OIII image

Figure 6.6: True colour image of H_α in red, H_β in blue, OIII in green done in IRAF and DS9

Preprints (www.preprints.org) | NOT PEER-REVIEWED | Posted: 5 September 2022 doi:10.20944/preprints202209.0070.v1

Figure 6.7: True colour image of H_α in red, H_β in blue, OIII in green done in Liberator 3 and Adobe Photoshop

 doi:10.20944/preprints202209.0070.v1

6.3 152 cm Telescope Data

The data and the reduction process is a bit different for the 152 cm telescope. Here the master flat image is a spectrum from a tungsten calibrating lamp, and master bias images are created together with one additional image that is then used for wavelength calibration. The name of this image is arch, and it contained an exposure from a thorium-argon calibration lamp. This will then be explained in wavelength calibration. These images will then have their 1D spectrum extracted. This is since the H_β is already extracted 1D spectra, the extraction process for all images can be viewed below. Next step after the extraction is to reduce them, which is done as before by Equation 6.1.

ecl> noao

noao> onedspec

onedspec> apextract

apextract> apall Master-flat.fits

"q" is pressed to quit plot for which series of settings will be displayed, answer to all of them is "yes". This will create a spectrum of .ms.FITS format. The 1D spectrum is then saved as a new spectrum by *imcopy* package; see bellow.

cl> imcopy master bias.ms.fits[*,1] master bias 1d.fits

To wavelength calibrate the spectroscopic data, an image; arch.fits is used. It is essentially a thorium-argon calibration lamp for which wavelength values are known. In theory, the wavelength calibration has three steps that go as follows, identify, refspec, dispcor. All processes are done for H_β (Spectrum in the 5000 Å) only. However, this procedure is exact for H_α (Spectrum in the 6499 Åband).

First is to use identify. To access this package a set of commands were carried out, those commands can be viewed below. This package allows us to manually identify lines and allocate them to actual arc lines. To make it easier the spectrum and the arc were cut so that just the three lines are included, which were sufficient enough for calibration. Table 6.1 shows what lines were used and their positions can be viewed in Figure 6.8.

ecl> noao

noao> onedspec

onedspec> idenify arc.fits

Preprints (www.preprints.org) | NOT PEER-REVIEWED | Posted: 5 September 2022 doi:10.20944/preprints202209.0070.v1

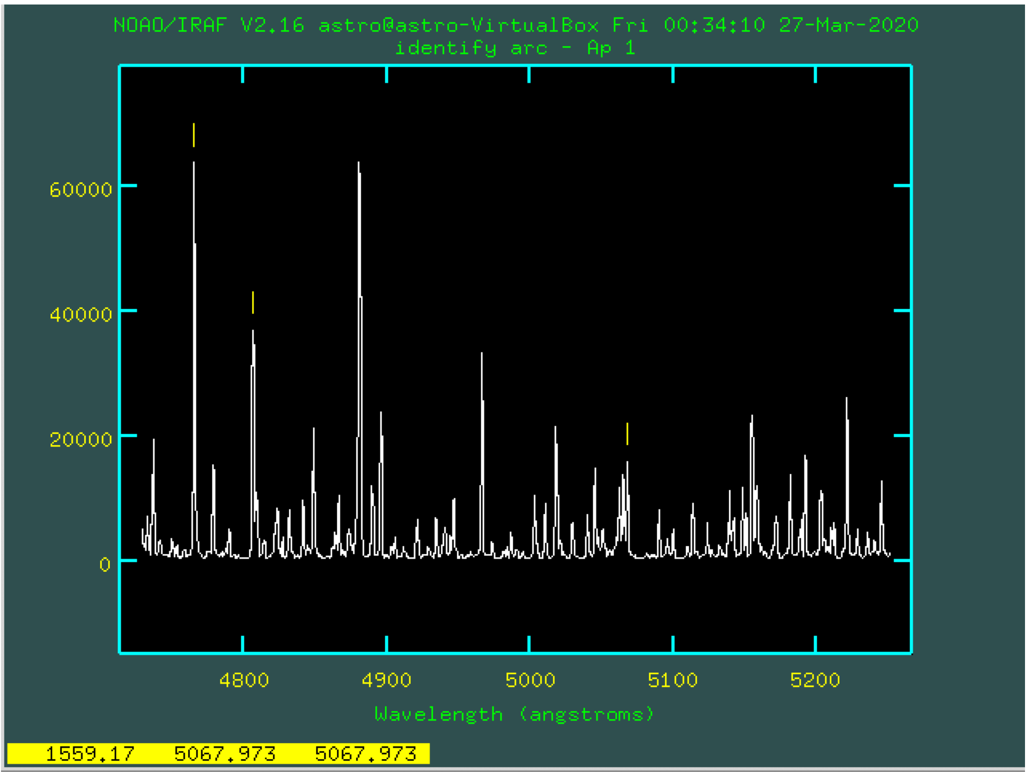

Figure 6.8: Thorium-argon lamp spectrum for H_β. Showing the lines which were identified.

Arc line
4764.89
4806.07
5067.97

Table 6.1: Arc lines selected

Next was identifying lines from H_β spectrum. This was done by pressing key "m", which allowed the wavelength to be inputted. The number of lines was identified this way. Pressing key 'f' was to fit the solution. The calibrations can be seen in Table 6.2.

Refspec is used after *identify* to make the calibrated arc spectrum the "reference spectrum" for the H_β spectrum. After that is finish dispcor, which is used to apply the calibration to the H_β spectrum. To view calibrated and reduced spectra, see Figure 6.12.

 doi:10.20944/preprints202209.0070.v1

pixel number	arc line
882.10	4764.89
974.21	4806.07
1559.21	5067.97

Table 6.2: Spectrum in the 5000 Åband line selected

 doi:10.20944/preprints202209.0070.v1

The next step was to reduce cosmic rays that are visible in DS9 Figure 6.9. This image represents a 2D H_β spectrum after reduction, three emission lines are visible and a bright spot in between the first two. This bright spot is cosmic rays that were detected by the telescope.

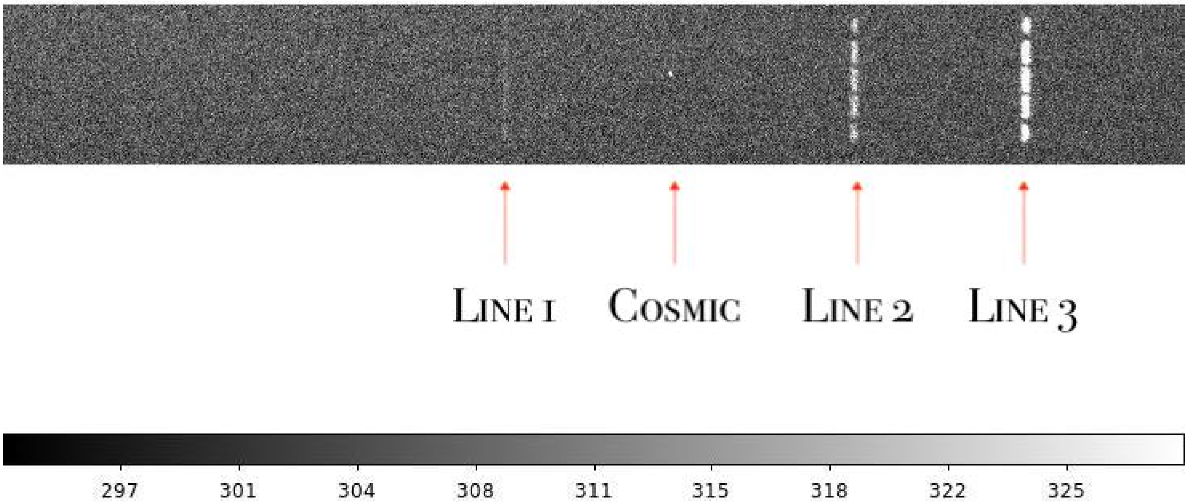

Figure 6.9: DS9 H_β 2D spectrum

As is visible in Figure 6.9 above, during data reduction a large number of cosmic rays were present in the 5000 Å band spectrum this scenario was same for the 6499 Å band spectrum. To manually correct for them function in *splot* was used. The idea was to fit a Gaussian, that was done by pressing key "k" around the unwanted lines, and then key "-" on each side, which then removed the line. Figure 6.10 and 6.11 shows the 6499 Å band spectrum with cosmic rays present and cosmic rays absent respectively (reduced spectra). Note that both are wavelength calibrated with a similar procedure that was done for the 5000 Å band spectrum. For the 5000 Å band, the reduced and calibrated spectra are to be seen in Figure 6.12 that shows the 5000 Å band spectra after reduction.

Preprints (www.preprints.org) | NOT PEER-REVIEWED | Posted: 5 September 2022 doi:10.20944/preprints202209.0070.v1

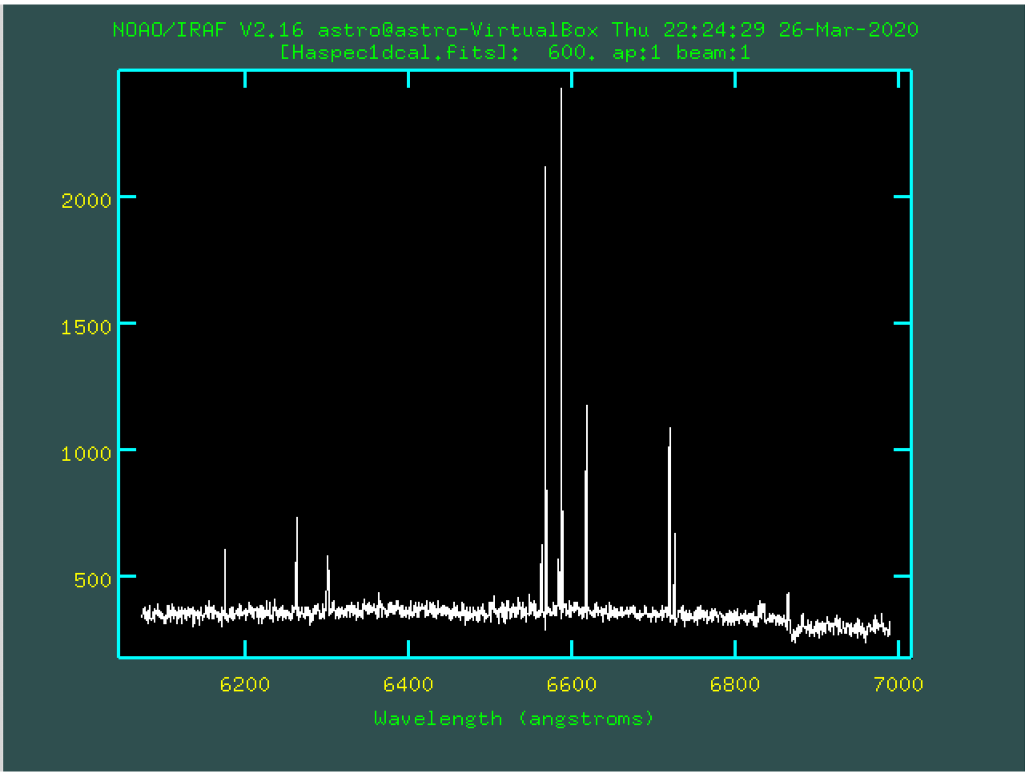

Figure 6.10: Spectrum in the 6499 Åband (with cosmic)

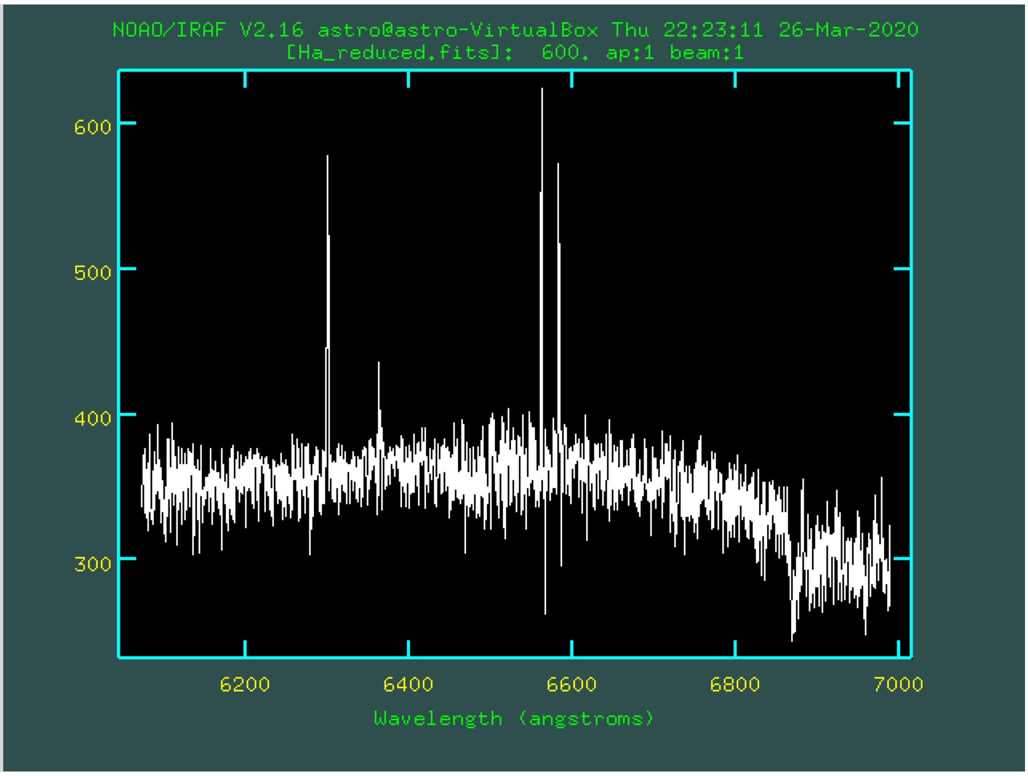

Figure 6.11: Spectrum in the 6499 Åband (without cosmic)

 doi:10.20944/preprints202209.0070.v1

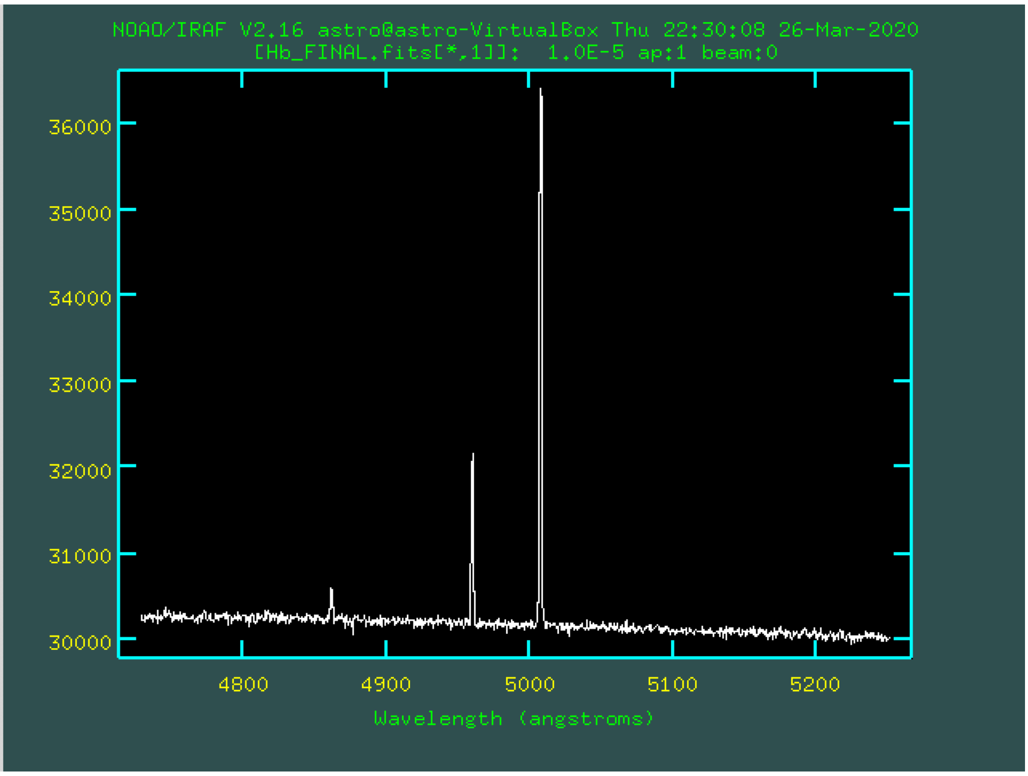

Figure 6.12: Spectrum in the 5000 Åband (without cosmic)

See the following Table 6.3 and Table 6.4 that represent the elements that were identified for the corresponding wavelength. These results are from the 6499 Å band and the 5000 Å band reduced and calibrated spectra respectively. For each a Gaussian was fit onto respective emission lines by pressing key “k” on each side of the line and the values were recorded.

Element	wavelength recorded	Counts
OI	6300.24	267.00
OI	6363.78	47.15
H_α	6562.23	471.9
NIII	6583.08	367.9

Table 6.3: H_α (data in the 6499 Å band.)

Element	wavelength recorded	Counts
H_β	4861.35	780.3
OIII	4959.61	3293
OIII	5007.48	10141

Table 6.4: H_β (data in the 5000 Å band.)

7 Flux Calibration

Flux Calibration was carried out using multiple tools such as Aperture Photometry Tool and IRAF. The main mathematical operation that is carried out on the image is done in IRAF. However, to flux calibrate an image, other resources such as finding standard star from surveys to have reference magnitude for each filter and executing photometry for gathering data about the state of the current image were both necessary before any mathematical operation.

7.1 Purpose of Flux Calibration

The purpose or goal is to tie image pixel values or counts to a standard physical system such as flux. The reason for flux is that it is a linear scale, not logarithmic like magnitudes, hence flux is the best choice for a standard system. When the image is eventually flux calibrated, a Balmer decrement is obtainable. Balmer decrement is a ratio of $\frac{H_\alpha}{H_\beta}$ that allows further progression for information gathering about the NGC 6853 such as temperature, densities, etc., provided that the scale is linear hence flux calibration of an image is vital.

7.2 Standard Stars

Photometric-standard stars are well known and measured stars. They have their light output in various passbands of the photometric system. Other objects such as the nebula NGC 6853 is then observed and compared to photometric-standard star for exact brightness, or stellar magnitude, of the object (Landolt 2000).

For this project, due to the lack of a standard star around the NGC 6853 nebula, another approach was taken. Using other methods which are discussed further below, three stars of known H_α values were found.

The first star named: TYC 2141-922-2 or HD 345468 depends on the catalogue, has celestial coordinates: [$\alpha = 19^h\ 59^m\ 20.7^s$, $\delta = +22^\circ\ 36'\ 51.86''$]. The H_α magnitude for this star was to be listed as 17.93 magnitude with an error of 0.02.

The second star named HD 345452 has celestial coordinates: [$\alpha = 19^h\ 59^m\ 59.5^s$, $\delta = +22^\circ\ 46'\ 29.56''$]. The H_α magnitude for this star was to be listed as 16.83 magnitude with an error of 0.01.

The third star named TYC 2141-1086-1 has a celestial coordinates: [$\alpha = 19^h\ 59^m\ 26.9^s$, $\delta = +22^\circ\ 38'\ 02.44''$]. The H_α magnitude for this star was to be listed as 18.03.

7.2.1 IPHAS

"The Isaac Newton Telescope (INT) Photometric H_α Survey of the Northern Galactic Plane (IPHAS) is a 1800-deg^2 CCD survey of the northern Milky Way spanning the latitude range $-5°$<b<$+5°$ and reaching down to $r \approx 20$" (Drew et al. 2005). The final catalog of IPHAS point sources will contain photometry on about 80 million objects. Used on its own, or in combination with near-infrared photometric catalogs, IPHAS is a significant resource for the study of stellar populations making up the disc of the Milky Way. This catalog was used to find desirable magnitudes of stars around the NGC 6853 nebula for a H_α filter (Drew et al. 2005).

7.2.2 Colour index

Due to a lack of surveys similar to the one like IPHAS for H_β, an idea was proposed by a thesis work on Comparison of H-alpha and H-beta Temperature Indices in the Hyades and Coma Star Clusters and Selected H-beta Standard Stars, by: (West 2010). Is that H_β color index being used as an indicator for temperature. The H_β color index for a star is calculated from the H_β and Vband magnitudes. The thesis finds a correlation between the H_α and H_β indices. The H_α index is calculated from the H_α magnitude and the Rband magnitude. The idea was to exploit the correlation between the indices, which then allow to work out the H_β index for the reference stars and thus the H_β magnitude. The correlation between the indices and hence the conversion from H_α to H_β is expressed in the sequence of the equation below:

$$H_\alpha C = R - H_\alpha \tag{7.1}$$

$$H_\beta = V - H_\beta C \tag{7.2}$$

$$H_\beta C = \frac{H_\alpha C - 0.487}{0.633} \tag{7.3}$$

The $H_\alpha C$ and $H_\beta C$ stands for H_α, H_β indices respectively, then R and V represent bands. The conversion started by obtaining the H_α indices. This was done by Equation 7.1. Next step was to use Equation 7.3 to obtain the H_β indices. Lastly, it was the conversion to H_β via Equation 7.2.

The calculated magnitudes for H_β are then: 11.090 for the second star [HD 345452] and 12.905 for the third star [TYC 2141-1086-1]. The first star was discarded due to over-saturation, more about this in the photometry section. The calculations gave an answer that showed a difference of magnitude between H_α and H_β approximately of 5 magnitudes. This is a substantial difference. Hence this method was found incorrect.

7.3 Photometry

Photometry in an astronomical image-data analysis that is an essential technique for measuring the brightness of a celestial object. Such as a star or galaxy or nebulae in case of this project. It is the calculation of source intensity by summing the measured counts from a sub-image containing the source (or possibly sources) and subtracting the sky background contribution estimated from a nearby imaged region that excludes the source of interest (Da Costa 1992).

7.3.1 Aperture Photometry Tool

Aperture Photometry Tool (APT) is a software for astronomers and students interested in manually exploring the photometric qualities of astronomical images. It is a graphical user interface (GUI) designed to allow the image data associated with aperture photometry calculations for point and extended sources to be visualized and, therefore, more effectively analyzed.

The idea behind aperture photometry is to fit a star with an aperture and measure the number of counts within that aperture. This is converted to an instrumental magnitude is done by the following formula, however this is done automatically by the software: (Vik Dhillon 2020)

$$m = Z_{mag} - 2.5 \log_{10}(F) + 2.5 \log_{10}(T_e) \tag{7.4}$$

Where F is flux and T_e time exposure, these parameters are in the .FITS file and there is no need to interact with them as the software is computing with them automatically, Z_{mag} is where the APT and IRAF differ.

Aperture Photometry Tool is computing all the parameters in the background. Hence, the only variation that is available for the program to be set correctly is the Z_{mag} or zero point in case of naming for APT. First, it was necessary to find the correct zero point. This was done by navigating into the APT software, under tools where a simple photometric-calibrations tool function is located. This function requires the user to create two .txt files, one that contains calibrated sources and one uncalibrated. For the calibrated sources, the .txt file was filed out as follows. Each row is designed for a single object; in this case, a star, columns are then as follows. The first column is the object's right ascension, the second column is declination, and the third column is the object's magnitude; for the calibrated file, this is then the object $H\alpha$ magnitude from IPHAS. Similarly, for the uncalibrated .txt file, however, this time the magnitudes are taken from the initial photometry that was run. When this was done the function gave a zero point value, this value was then taken and rewritten in APT settings, photometry then followed now with corrected magnitudes of the objects.

For the project, two stars were used to calibrate zero point, The second star (HD 345452), and the third star (TYC 2141-1086-1). These stars calibrated values for $H\alpha$ are from IPHAS catalog. Here they were given as 16.83 and 18.03 respectively, and the uncalibrated values from initial photometry were -14.27 and -15.60, respectively. The resulting zero point was 32.36. This value was taken and used in settings to change the zero point. And after doing that, the photometry was recomputed, and the new magnitudes were 16.76 and 18.09, respectively. This was assumed to be close enough for the purpose, and now the APT is calibrated for correct readings.

In the next step, more results such as, source scatter which is an indicator for a stars saturation, and counts in the aperture that was set to a circle, with a radius of nine pixels. The graphs for second star (HD 345452) and third star (TYC 2141-1086-1) are visible in Figure 7.1 and 7.2 respectively. Here, it was found that the first star (TYC 2141-922-2 or HD 345468) was oversaturated, hence, it was discarded. The counts were recorded to be 1.79×10^6 and 592178 for second star (HD 345452) and third star (TYC 2141-1086-1), respectively. A similar procedure was done for H_β.

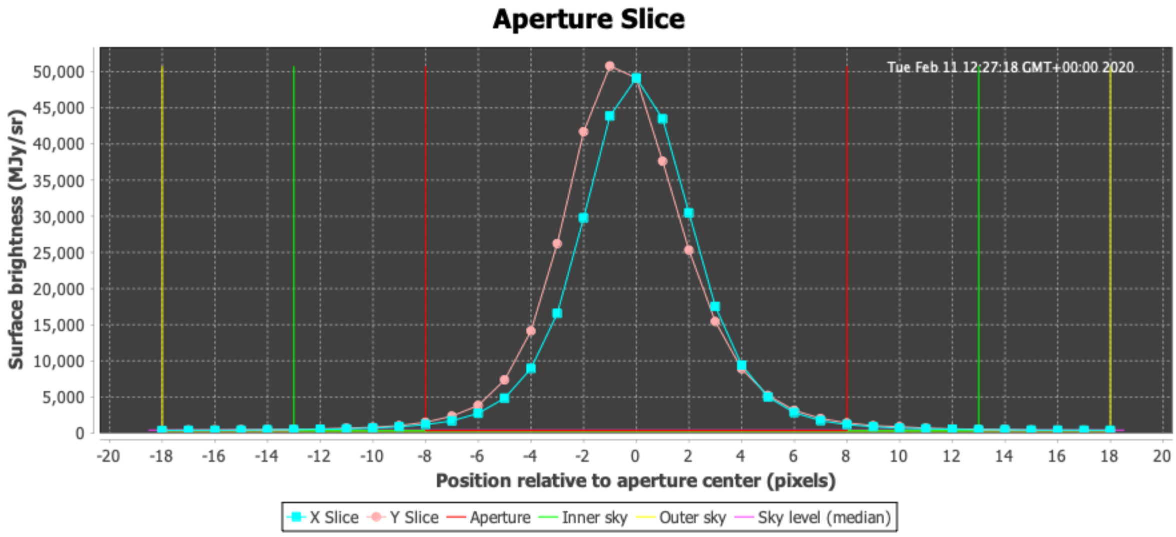

Figure 7.1: source scatter for second star (HD 345452)

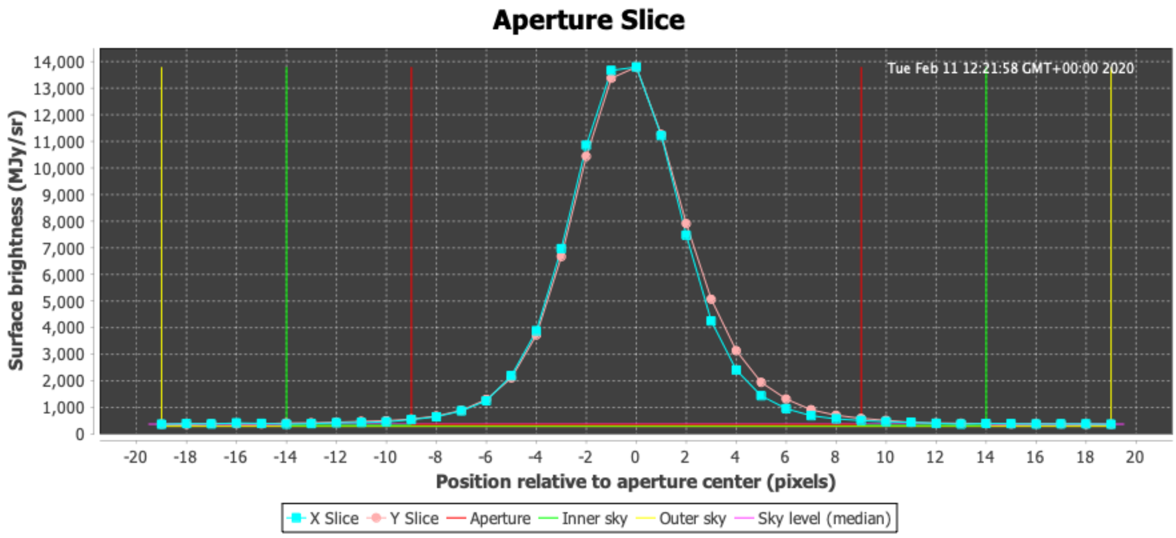

Figure 7.2: source scatter for third star (TYC 2141-1086-1)

7.3.2 IRAF

This is where the IRAF differs compared to the APT. When the photometry is done on IRAF using PHOT, the result that is given is then the instrumental magnitude, which is not the actual magnitude of the celestial object. To further calculate the actual magnitude, which is the difference of some calibration factor between the instrumental and actual magnitudes (δ_m) has to be incorporated into the instrumental magnitude result. This is done by finding a few standard or reference stars that have known magnitudes, again IPHAS can be use for this. Then work out their instrumental magnitudes and work out δ_m. For each reference star, δ_m should be the same within errors.

Preprints (www.preprints.org) | NOT PEER-REVIEWED | Posted: 5 September 2022 doi:10.20944/preprints202209.0070.v1

On IRAF the instrumental magnitude and counts for the second star (HD 345452) and third star (TYC 2141-1086-1) were done, as APT was used instead. However, example of how the instrumental magnitude was made can be seen below:

ecl> noao

noao> digiphot

digiphot> apphot

First step was to navigate IRAF into the new directory that contained PHOT. How that was done is visible above. Next step was to set up the PHOT settings, which were approached by a command listed below. Further hidden parameters that needed to be modified were reached by a command ":e" that was typed into the subsections to display those extra parameters where setting like aperture size can be modified.

cl> epar phot

To run PHOT, a series of commands below were followed. First was to display the .FITS file that needed to be analyzed. This then followed by executing PHOT command that caused the cursor to turn black, this black dot was positioned on the star of interest and space bar was pressed. At this point photometry was conducted and table of stars saturation is displayed together with the star magnitude and the number of counts inside the aperture. A key "q" was pressed two times to save the graph together with all the data that PHOT can reproduce. To then view that data a new save file named .FITS.MAG is opened, and on line five the sum of counts inside the aperture is listed, and line six is then the magnitude, which was found to be 9.464 and 10.80 for the second star (HD 345452) and third star (TYC 2141-1086-1) respectively, the counts did not change compared to APT which is expected. A similar process was done for H_β.

cl> display Halpha_final.fits

cl> phot Halpha_final.fits

Preprints (www.preprints.org) | NOT PEER-REVIEWED | Posted: 5 September 2022 doi:10.20944/preprints202209.0070.v1

7.4 Calibration trials

7.4.1 Counts to magnitude by galaxy magnitude approach

One of the trials to flux calibrate the H_α and H_β was with the following Equation 7.5, this equation required the magnitude of the reference star (mag_{ref}), counts of the reference star (f_{ref}), the image (f_{image}) and the pixel area (pix^2).

The pix^2 was found by knowing the value of the pixel size, the f_{ref} was found using aperture photometric tool, the mag_{ref} was found from a IPHAS catalog see Section 7.2.1 for H_α and for H_β value that was calculated see Section 7.2.2 which was probably the cause for this approach to be incorrect.

$$mag_{nebula} = -2.5 \log \frac{f_{ref}}{\frac{f_{image}}{pix^2}} + mag_{ref} \tag{7.5}$$

7.4.2 Counts to Flux by telescopes conversion tool approach

Aperture photometric tool, see Section 7.3.1 is used to gather required values from each reference star, the counts, the size of the aperture in pixels, and the magnitudes that are corrected to the known values from a IPHAS for H_α, see Section 7.2.1. These values are then used in the conversion tool provided by Gemini telescopes (*Conversion from magnitudes to flux, or vice-versa | Gemini Observatory* 2020), to obtain the flux of each reference star in units of W/m^2. At this point the following values are known; the magnitude of the star, the flux of the star, the area of the aperture and the counts of the star.

The next step was to calculate the factor which allows the conversion from counts to $flux$ per $area^2$ for each reference star. This was done by dividing the flux that was obtained from the tool by the area of the aperture. This then gives the relation between counts that is equal to flux per $area^2$ in pixel, since the targeted unknown is the flux per pixel the flux per $area^2$ was then divided again by the count which gives the final value of flux per pixel, however, what is required is the scaling factor of this value, so if the answer looks like 5.64×10^{-36} then the scaling factor is the 5.64.

This method was once again incorrect, due to the H_β value that was calculated, see Section 7.2.2. At this point, the flux calibration was abandoned. Nevertheless, the image can still be calibrated, and this is then done in Section 8.1.

8 Results and Discussion

8.1 254 cm Results

Regardless of the multiple trials that are described in Section 7 above, the image from the 254 cm telescope was unable to be flux calibrated due to the lack of known H_β values from a standard star. The next possibility that was used is the known interstellar reddening relationship. This is then used to calibrate the image due to the fairly confident values of the H_α that were obtained. See the following Equations 8.2 and 8.3 that give the relation between $\frac{H_\alpha}{H_\beta}$ and reddening (Giammanco et al. 2011).

$$R_v = \frac{A_V}{E(B-V)} \tag{8.1}$$

$$A_V = 2.15 \times c_\beta \tag{8.2}$$

$$c_\beta = 2.84 \times \log \frac{H_\alpha/H_\beta}{2.86} \tag{8.3}$$

The idea behind this method is to use the c_β, which can be obtained by rearranging Equation 8.2 and using its relation to find a scaling factor for H_β. The first step was to find the A_V (visual extinction), for that the ratio of total to selective extinction was used, see Equation 8.1. According to (Bohlin, Harrington, and Stecher 1982) the colour excess, E(B-V) of NGC 6853's central star is 0.06 and according to (Pottasch et al. 1977) the colour excess of the nebula is 0.10 $\pm$ 0.04. These values are in agreement with each other. However, the color index obtained from Pottasch is chosen, as using the color index from the central star is not 100 % accurate. The value for R_v was assumed to be 3.1, which is a typical value of extinction ratio for the B-band to V-band. Using these R_v and E(B-V) values and rearranging the Equation 8.1 for A_V ,it was then calculated to be 0.31.

Preprints (www.preprints.org) | NOT PEER-REVIEWED | Posted: 5 September 2022 doi:10.20944/preprints202209.0070.v1

Using the A_V value and applying Equation 8.2 value for c_β was calculated to be 0.1442. The H_β scaling factor that is obtained from Equation 8.3 (where the 2.86 is the theoretical Balmer ratio fo 12,000 K), was then obtained by picking a point on the nebula that is quite diffuse and faint. This allows us to assume that the nebula is not absorbing any of its own emission. Here, the c_β obtained from above together with the value of H_α at that point will determine what H_β should be at that point. Last is then to scale the H_β image by Equation 8.4 to match. This method gives a good approximation of the $\frac{H_\alpha}{H_\beta}$ map around the nebula that can be seen in Figure 8.1 bellow.

$$H_\beta = H_\alpha(0.311) \tag{8.4}$$

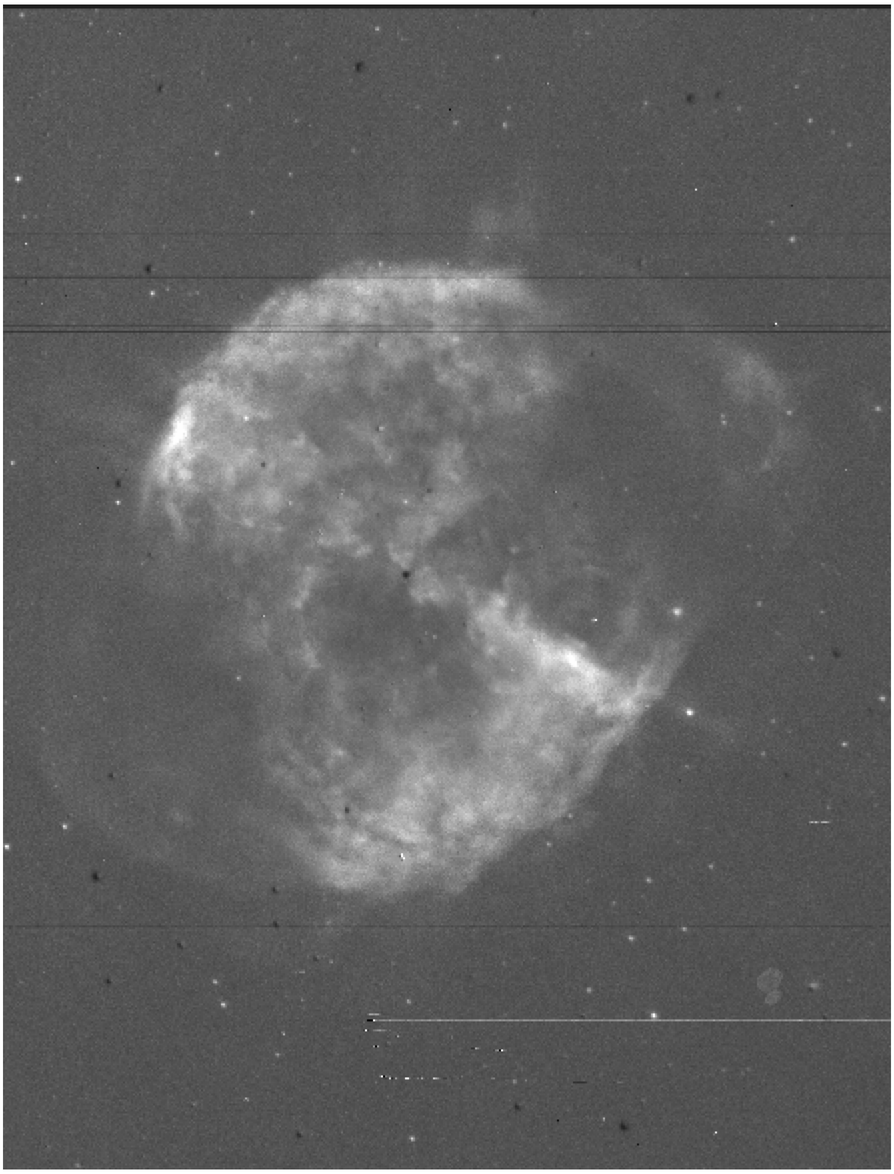

Figure 8.1: Calibrated division image of H_α and H_β

There were two simple cases for the nebula that were considered. One where the density of the cloud was homogeneous throughout, with only the temperature varying and the other where the temperature was homogeneous throughout the cloud and only the density changing.

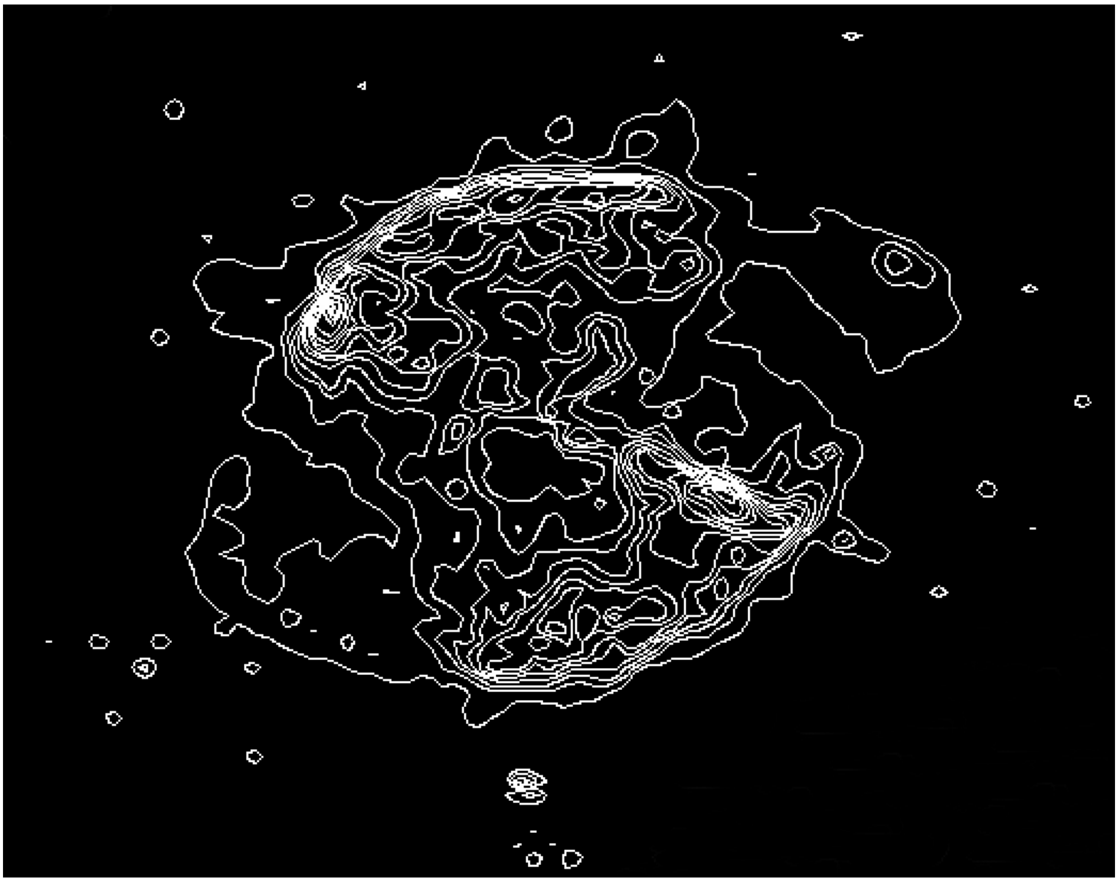

Figure 8.2: Contour plot showing the ranging values of differing $\frac{H_\alpha}{H_\beta}$

In Figure 8.2 it is possible to see the varying regions of differing "intensity" which correspond to the bright spots in Figure 8.1. The more compact "lines" indicate regions of interest due to the considerable variation compared to the surrounding environment.

8.1.1 Homogeneous Density

By assuming that the density is consistent throughout the nebula, differences of the ratio between H_α and H_β can be assigned to higher temperatures. Theoretical value of 2.86 for 12,000 K (Bohuski, Dufour, and D. Osterbrock 1974) is expected. However, recorded values from Figure 8.1 are in the range of 2.8 for diffuse and faint regions and just below 8.1 for the dense regions, these extreme values would result in nebula's temperature being 50,000 K +, which are entirely unrealistic

 doi:10.20944/preprints202209.0070.v1

results. It was therefore necessary to consider not a homogeneous density but a constant temperature and varying density.

8.1.2 Homogeneous Temperature

Since assumption above is giving extreme values that are unrealistic, by assuming that the temperature is constant throughout the nebula (12,000 K) and the variations in Figure 8.3 and 8.2 are caused only by the density changing, it is still possible to model the structure of the nebula and apply a morphological study. The procedure is discussed below.

The concept of the column density of a neutral hydrogen atom is a measure of the amount of intervening matter between the observer and object that is being observed along a particular line of sight. However, to construct a map of varying density two major assumptions had to be taken into consideration (*Column Density | COSMOS* 2020).

First, it is assumed that the with of the emission region is to be the radius of the nebula in cm. This is then for NGC 6853 the radius (R) and is equal to 1.3623×10^{18} cm (Terzian 1966). The second assumption is that the majority of the nebula is within the region R. When this assumption holds then the resulting map will display a value at chosen points which then gives a value in terms of atoms per cm^3.

The color excess A_V is the difference between its "laboratory color index", and its observed color index, then the total extinction (A_V) and the column density of neutral hydrogen atoms N_H are related by:

$$N_H = 1.8 \times 10^{21} \times A_V \ cm^{-2} \ mag^{-1} \tag{8.5}$$

The observed colour index (c_β) that can be obtained by using Equation 8.3 for which this time the $\frac{H_\alpha}{H_\beta}$ is the calibrated image. The color excess (A_V) was then obtained from Equation 8.2, however, this was not the final A_V value, as the ISM background absorption that was calculated to be 0.31 previously had to be taken away so that only the nebula's color excess is considered, this was then named $A_V r$ for reduced.

These steps were undertaken in *IRAF* by using the following packages. For mathematical scaling of the image, *imarith* was used, and *imfunction* for application of a logarithm onto the image. This had to be done in steps; hence the naming later, the procedures are displayed below. However, for the final step, a Python script was written which converted and plotted the reduced color excess

Preprints (www.preprints.org) | NOT PEER-REVIEWED | Posted: 5 September 2022 doi:10.20944/preprints202209.0070.v1

($A_V r$) to density by using the relationship displayed in Equation 8.5 and dividing it by its radius (R). Equation 8.6 shows final density formula and Figure 8.3 shows the contour plot generated by it. The following Figure 8.4 is a contour plot that is done from a data set collected at the 120 cm telescope from OHP France and was analyzed by (M.Birney 2020).

These two results are then compared with each other. The actual Script can be then seen in Appendix B.1.

$$Density = \frac{A_V r}{R}\ atoms\ /\ cm^3 \tag{8.6}$$

ecl> imarith HaHb.fits / 2.86 1st.fits

ecl> imfunction 1st.fits 2nd.fits log10

ecl> imarith 2nd.fits * 2.84 3rd.fits

ecl> imarith 3rd.fits * 2.15 Av.fits

ecl> Av.fits - 0.31 Avr.fits

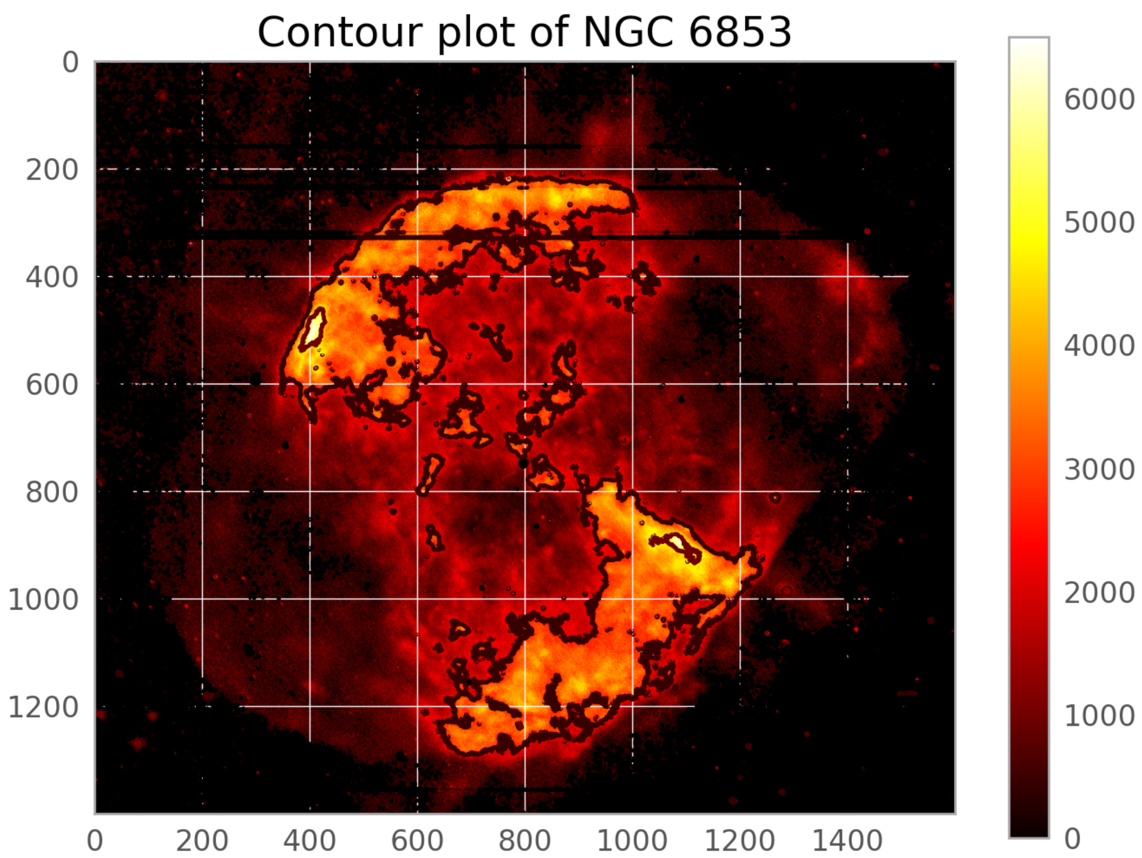

Figure 8.3: Contour plot generated in Python with different levels corresponding to different values for the density in atoms per cm^3 254 cm telescope

Preprints (www.preprints.org) | NOT PEER-REVIEWED | Posted: 5 September 2022 doi:10.20944/preprints202209.0070.v1

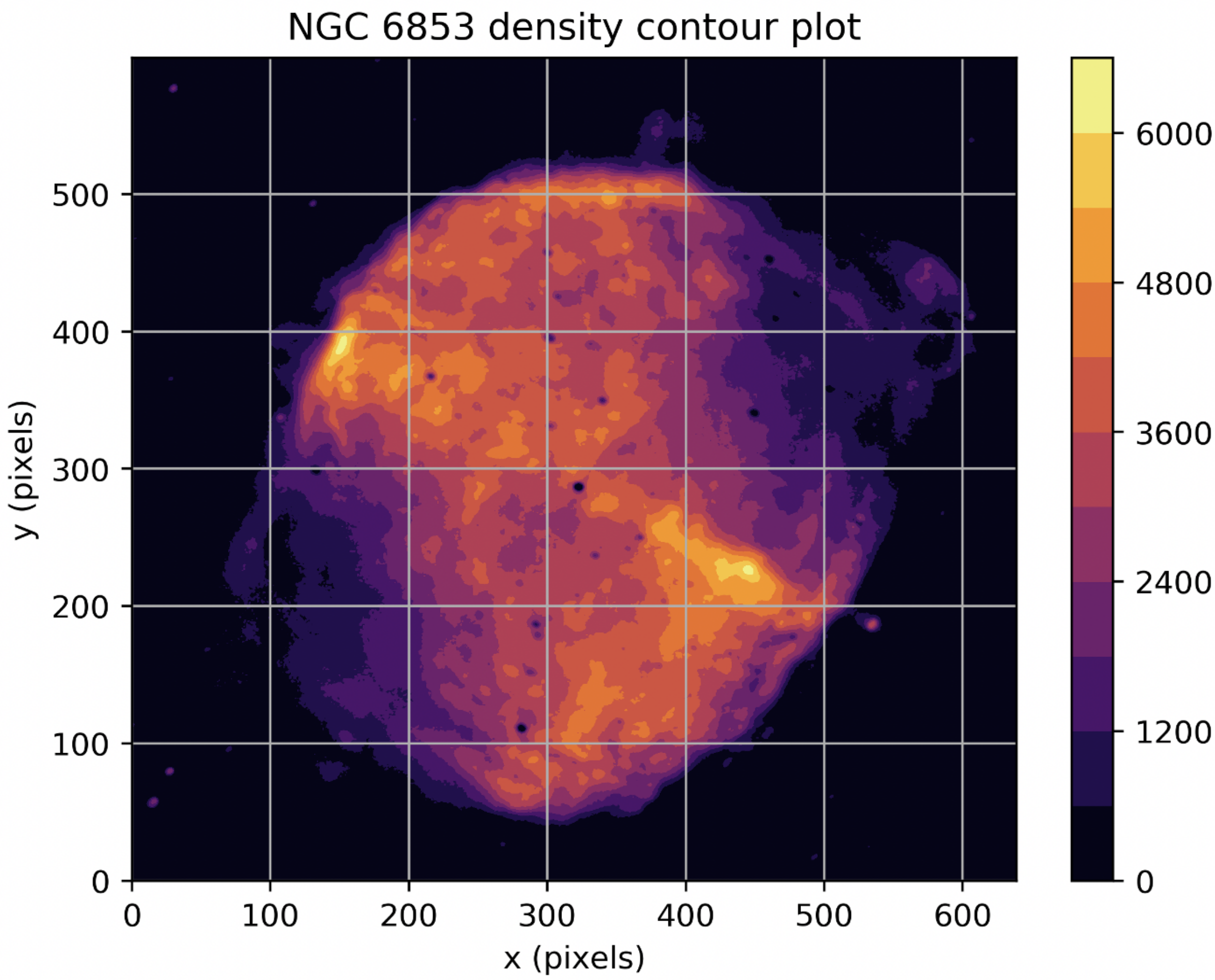

Figure 8.4: Contour plot generated in Python with the different levels corresponding to different values for the density in atoms per cm^3 120 cm telescope

The structure of the nebula can be seen clearly, with two extremely dense regions at (500,500), (1100,900) and (150,380), (440,200) for Figure 8.3 and Figure 8.4 respectively. The positions and values of these dense lobes displayed in the plots sort of agree but the data from INT shows a slightly lower density by ≈ 2000 atoms per cm^3.

To further check for values of density (ρ) at multiple selected positions, a python script was written. To view the script see Appendix B.2. The range of values for ρ that are shown in Figure 8.5 are given in Table 8.1 and quoted $\pm\ 3\sigma$, where σ was calculated by:

$$\sigma = \sqrt{\frac{\sum (X - \overline{X})^2}{n}} \tag{8.7}$$

Where all symbols have their usual meanings.

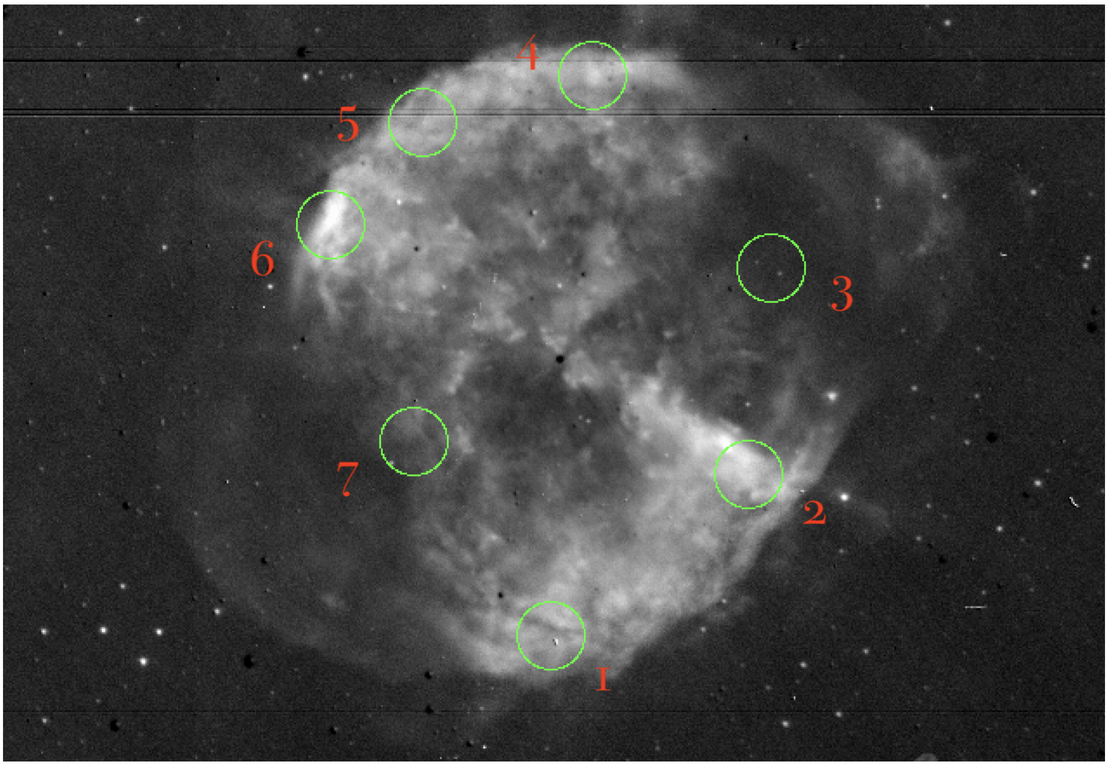

Figure 8.5: Selected points on the nebula where the density was calculated

Region	ρ (atoms cm^{-3})
1	2769.00 ± 228.98
2	6019.00 ± 228.97
3	376.63 ± 228.97
5	3480.71 ± 228.85
6	6441.11 ± 228.90
7	1071.97 ± 229.86

Table 8.1: Density of NGC 6853 corresponding to those in Figure 8.5

The data of the dense lobes displayed in the plots agrees with the values from Regions 2 and 6 in Table 8.1. And the particle densities obtained are in accordance with typical nebular densities (Donald E Osterbrock and Ferland 2006). The representation of uniformly localized density through the nebula can be see in Figures 8.3 and 8.4 or in the Table 8.1 above, where the regions 6,5 & 4 on one side of the nebula and regions 1 & 2 on the other side indicate regions of higher density.

 doi:10.20944/preprints202209.0070.v1

This is characteristic dumbbell shape is due to fast stellar winds carved out cavities in the spherically symmetric winds remnants creating the bipolar dumbbell shape. High density knots and highly collimated bipolar outflows or jet-like structures from central star.

However, despite the density of the region being known, it is not known where these dense regions are exactly located; whether it is uniform throughout the whole nebula or localized in a single region.

(Hartmann and MacGregor 1982) proposed that the highest region of outflow of an orbit is in the equatorial plane, as the centrifugal and magnetic forces are at their largest.

 doi:10.20944/preprints202209.0070.v1

8.2 152 cm Results

The emission lines that were detected on the 152 cm telescope were used to estimate the radial velocity (v_{rad}) of the nebula and the expansion velocity (v_{exp}) of the nebula.

The v_{rad} is estimated by fitting a Gaussian distribution upon the line in *splot*, which is an *IRAF* package for spectra analysis. However, to obtain the v_{rad} in units of kms^{-1}, the Gaussian is plotted by pressing key "k" on each side of the line and then by pressing key "v" the scale changes to desired units. The value that is the center of the Gaussian is the radial velocity (v_{rad}) of the nebula, see Table 8.2 for the 6499 & 5000 Åbands.

For the expansion velocity (v_{exp}), exact same procedure as described above, however this time the value that represents FWHM is divided by 2 which results in obtaining HWHM that represents the expansion velocity (v_{exp}) of the nebula. See Table 8.2 for the 6499 & 5000 Å bands.

The error on the wavelengths was calculated by finding one standard deviation for the Gaussian:

$$\sigma = \frac{FWHM}{2.3548\sqrt{N}} \tag{8.8}$$

Where σ is the standard deviation on the wavelength, FWHM is the full-width half maximum of the Gaussian and N is the absolute value of the counts in the line.

The error for the radial velocity (v_{rad}) for the 6499 & 5000 Å bands were calculated by applying the calibration back onto itself, and comparing the accepted wavelengths with the calibrated wavelengths. See Equation 8.9. This gave a value of δv_{rad}, which is then applied to Equation 8.10. Resulting Equation 8.11 was then assumed for both of the 6499 & 5000 Å bands lines.

$$\delta v_{rad} = \frac{\lambda_{calibrated} - \lambda_{accepted}}{\lambda_{accepted}} \times c \tag{8.9}$$

$$\Delta v\ error = \pm \frac{\delta v_{rad_1}^2 + \delta v_{rad_2}^2 + .. + \delta v_{rad_n}^2}{n} \tag{8.10}$$

$$\Delta v = \pm\ 0.38\ kms^{-1} \tag{8.11}$$

8.2.1 Nebular Cloud

In the nebular cloud the emission lines that were observed can be see in Tables 6.4 & 6.3 for 6499 Å & 5000 Å bands respectively.

	Observed Wavelength (Å)	Rest Wavelength(Å)	v_{exp} (km/s)	v_{rad} (km/s)
H_β	4861.35 ± 0.014	4861.36	54.40 ± 0.38	-23.70 ± 0.38
OIII	4959.60 ± 0.006	4958.91	43.87 ± 0.38	-15.80 ± 0.38
OIII	5007.48 ± 0.003	5006.84	42.68 ± 0.38	-18.27 ± 0.38
OI	6300.24 ± 0.026	6300.30	17.03 ± 0.38	-37.38 ± 0.38
OI	6363.78 ± 12.183	6363.78	27.50 ± 0.38	37.07 ± 0.38
H_α	6562.23 ± 0.011	6562.80	34.66 ± 0.38	-91.79 ± 0.38
NIII	6583.08 ± 0.033	6730.82	41.66 ± 0.38	-56.70 ± 0.38
		mean values	37.40 ± 0.38	-29.50 ± 0.38

Table 8.2: Results of spectroscopy in 5000 Å & 6499 Å bands for the nebular cloud, where the v_{exp} was obtained from reading the center value of Gaussian, and v_{exp} was obtained from the HWHM value of the Gaussian.

The mean radial velocity for all lines was calculated to be -29.50 ± 0.38 kms^{-1}, and the mean expansion velocity was calculated to be 37.40 ± 0.38 kms^{-1}. The lines were found to be blue shifted which tells that they are moving towards us, and the nebula is constantly expanding in volume. The obtained result for the radial velocity does not agree with the calculated radial velocity -45 ± 2 kms^{-1} that was done by (Doroshenko 1971). However the the expansion velocity does fall within the range of [30 - 90] kms^{-1} that was done by (Doroshenko 1971).

9 Conclusions

The aim of this project was to perform analysis on the planetary nebula NGC 6853 from 254 cm telescope and compare its results to its 120 cm telescope. More specifically, to perform and compare temperature mapping of the nebulae regions together with a morphological study of the nebulae density in those varying regions. Observations of the nebula demonstrate its forbidden lines [OIII] doublet along with H_α and H_β and many more emission lines. See section 8.2 for more. The structure and shape of the nebula can be seen in section 6.2 or more detailed in section 8.1.2, with two distinct high dense regions for both cases.

The project failed to find the temperature due to the incorrect calibration of H_β image in both cases; hence the theoretical Balmer decrement value which was 2.86 for 12,000 K (Bohlin, Harrington, and Stecher 1982) was used.

The density of the nebula was found to range from 376.63 $\pm$ 228.97 atoms per cm^3 to 6441.11 $\pm$ 228.90 atoms per cm^3 in various regions throughout the nebula. These different regions may be caused through material disposing from the central star on its equatorial plane, as mentioned in section 8.1.2. The values from the 254 cm telescope were slightly lower by $\approx$ 2000 atoms per cm^3 for the extremely dense region when compared to the analyzed results from 120 cm telescope (same region). If further investigation would be done on the [OIII], [OI] and NIII lines more detailed analysis of the dense regions would be possible.

The radial velocity was found to be blue shifted and calculated to be -29.50 $\pm$ 0.38 kms^{-1}, which was lower than usual. See Section 8.2.1 for more. Furthermore, the nebulae were found to be expanding in volume, and its expansion velocity was calculated to be 37.40 $\pm$ 0.38 kms^{-1}, which does agree with the usual. See section 8.2.1 for more.

References

Benedict, G Fritz et al. (2003). "Astrometry with the Hubble Space Telescope: A parallax of the central star of the Planetary Nebula NGC 6853". In: *The Astronomical Journal* 126.5, p. 2549.

Benedict, G. et al. (Dec. 2007). "Astrometry with The Hubble Space Telescope: A Parallax of the Central Star of the Planetary Nebula NGC 6853". In: *The Astronomical Journal* 126, p. 2549. DOI: 10.1086/378603.

Bohlin, RC, JP Harrington, and TP Stecher (1982). "International Ultraviolet Explorer observations of the central stars of the planetary nebulae NGC 6853 and NGC 7293". In: *The Astrophysical Journal* 252, pp. 635–643.

Bohuski, TJ, RJ Dufour, and DE Osterbrock (1974). "Nebular photometry with an echelle spectrometer:[O III] line ratios in NGC 1976 and NGC 6853." In: *The Astrophysical Journal* 188, pp. 529–532.

Column Density | COSMOS (2020). URL: http://astronomy.swin.edu.au/cosmos/C/Column+Density (visited on 04/03/2020).

Conversion from magnitudes to flux, or vice-versa | Gemini Observatory (2020). URL: https://www.gemini.edu/sciops/instruments/midir-resources/imaging-calibrations/fluxmagnitude-conversion (visited on 04/06/2020).

Da Costa, GS (1992). "Astronomical CCD Observing and Reduction Techniques (ASP Conf. Ser. 23), ed". In: *SB Howell (San Francisco, CA: ASP)* 90.

Doroshenko, VT (1971). "Velocity Field of the Planetary Nebula NGC 6853." In: *Soviet Astronomy* 15, p. 358.

Draine, Bruce T (2010). *Physics of the interstellar and intergalactic medium.* Princeton University Press.

Drew, Janet E et al. (2005). "The INT photometric Hα survey of the northern Galactic plane (IPHAS)". In: *Monthly Notices of the Royal Astronomical Society* 362.3, pp. 753–776.

Formation of Planetary Nebulae (2020). URL: https://www.cosmotography.com/images/planetary%7B%5C_%7Dnebula%7B%5C_%7Dformation.html (visited on 02/16/2020).

Giammanco, Corrado et al. (2011). "IPHAS extinction distances to planetary nebulae". In: *Astronomy & Astrophysics* 525, A58.

Gillet, D et al. (1994). "AURELIE: the high resolution spectrometer of the Haute-Provence Observatory." In: *Astronomy and Astrophysics Supplement Series* 108, pp. 181–192.

Griffiths, Martin (2012). *Planetary Nebulae and how to observe them*. Springer Science & Business Media.

Gurzadyan, Grigor A (2013). *The physics and dynamics of planetary nebulae*. Springer Science & Business Media.

Hartmann, LMKB and KB MacGregor (1982). "Protostellar mass and angular momentum loss". In: *The Astrophysical Journal* 259, pp. 180–192.

Howell, Steve B (2006). *Handbook of CCD astronomy*. Vol. 5. Cambridge University Press.

Hummer, DG and PJ Storey (1987). "Recombination-line intensities for hydrogenic ions–I. Case B calculations for H I and He II". In: *Monthly Notices of the Royal Astronomical Society* 224.3, pp. 801–820.

Isac Newton Group of Telescopes (2020). *Public Information on INT*. URL: http://www.ing.iac.es/PR/int%7B%5C_%7Dinfo/ (visited on 03/04/2020).

Janesick, James R (2001). *Scientific charge-coupled devices*. Vol. 83. SPIE press.

Kwok, Sun (2007). *The origin and evolution of planetary nebulae*. Cambridge University Press.

Landolt, AU (2000). "VizieR Online Data Catalog: UBVRI Photometric Standards (Landolt 1992)". In: *VizieR Online Data Catalog* 2183.

Marquez, Maria Jose (2012). "A Bayesian approach to the inference of parametric configuration of the signal-to-noise ratio in an adaptive refinement of the measurements". In: *arXiv preprint arXiv:1208.2048*.

Napiwotzki, Ralf (1999). "Spectroscopic investigation of old planetaries IV. Model atmosphere analysis". In: *arXiv preprint astro-ph/9908181*.

Observatoire de Haute-Provence (OHP) (2020). URL: http://www.obs-hp.fr/welcome.shtml (visited on 04/01/2020).

Osterbrock, Donald E and Gary J Ferland (2006). *Astrophysics Of Gas Nebulae and Active Galactic Nuclei*. University science books.

Planetary Nebulae | www.cfa.harvard.edu/ (2020). URL: https://www.cfa.harvard.edu/research/oir/planetary-nebulae (visited on 02/13/2020).

Pottasch, SR et al. (1977). “Ultraviolet observations of planetary nebulae. I-Determination of extinction”. In: *Astronomy and Astrophysics* 54, pp. 435–442.

RGO (2020). *Photos of the INT.* URL: http://www.ing.iac.es/PR/archive/int/int3.html (visited on 03/04/2020).

Ridpath, Ian (2012). *A dictionary of astronomy.* Oxford University Press.

Seaton, M. J. (Apr. 1954). “Electron Temperatures and Electron Densities in Planetary Nebulae”. In: *Monthly Notices of the Royal Astronomical Society* 114.2, pp. 154–171. ISSN: 0035-8711. DOI: 10.1093/mnras/114.2.154. URL: https://academic.oup.com/mnras/article-lookup/doi/10.1093/mnras/114.2.154.

Shapiro, Stuart L and Saul A Teukolsky (2008). *Black holes, white dwarfs, and neutron stars: The physics of compact objects.* John Wiley & Sons.

Sindhu, PS (2006). *Fundamentals of Molecular Spectroscopy.* New Age International.

Swinburne University | Melbourne, Australia (2020). URL: https://www.swinburne.edu.au/ (visited on 03/02/2020).

Terzian, Yervant (1966). “Radio emission from planetary nebulae”. In: *The Astrophysical Journal* 144, p. 657.

The Dumbbell Nebula (NGC 6853, M27) (2020). URL: https://www.cosmotography.com/images/small%7B%5C_%7Dngc6853.html (visited on 03/03/2020).

Tlescope de 1m52 OHP (n.d.). URL: http://www.obs-hp.fr/guide/152.html.

University, The Open (2020). *Astronomy with an online telescope: 3.2 The Altitude-Azimuth system - OpenLearn - Open University - AOT_1.* URL: https://www.open.edu/openlearn/ocw/mod/oucontent/view.php?id=96046%7B%5C&%7Dsection=%7B%5C_%7Dunit2.3.2 (visited on 02/28/2020).

Vik Dhillon (2020). *vik dhillon: phy217 - instruments - photometers - calibrating photometric data.* URL: http://www.vikdhillon.staff.shef.

 doi:10.20944/preprints202209.0070.v1

ac.uk/teaching/phy217/instruments/phy217%7B%5C_%7Dinst%7B%5C_%7Dphotcal.html (visited on 03/19/2020).

West, Miriam Anne (2010). "Comparison of H-alpha and H-beta Temperature Indices in the Hyades and Coma Star Clusters and Selected H-beta Standard Stars". In.

Preprints (www.preprints.org) | NOT PEER-REVIEWED | Posted: 5 September 2022 doi:10.20944/preprints202209.0070.v1

Appendix A Observational Logs

Date	S.time	Exp.	Object	Ra	Dec	F.	Bin	Comments
161019	18:27	300	NGC6853	19 59 40	22 42 31	Hb	2	Noise
161019	18:27	300	NGC6853	19 59 40	22 42 31	Hb	2	Noise
161019	18:27	300	NGC6853	19 59 40	22 42 31	Hb	2	Noise
161019	18:27	300	NGC6853	19 59 40	22 42 31	Hb	2	Noise
161019	18:27	300	NGC6853	19 59 40	22 42 31	Hb	2	Noise
161019	18:27	300	NGC6853	19 59 40	22 42 31	Hb	2	Noise
161019	18:27	300	NGC6853	19 59 40	22 42 31	Hb	2	Noise
161019	18:27	300	NGC6853	19 59 40	22 42 31	Hb	2	Noise
161019	18:27	300	NGC6853	19 59 40	22 42 31	Hb	2	Noise
161019	18:27	300	NGC6853	19 59 40	22 42 31	Hb	2	Noise
161019	18:27	300	NGC6853	19 59 40	22 42 31	Hb	2	Noise
161019	18:27	300	NGC6853	19 59 40	22 42 31	Hb	2	Noise
161019	18:27	300	NGC6853	19 59 40	22 42 31	Hb	2	Noise
161019	18:27	300	NGC6853	19 59 40	22 42 31	Hb	2	Noise
161019	18:27	300	NGC6853	19 59 40	22 42 31	Hb	2	Noise
161019	18:27	300	NGC6853	19 59 40	22 42 31	Hb	2	Noise
161019	18:27	300	NGC6853	19 59 40	22 42 31	Hb	2	Noise
161019	18:27	300	NGC6853	19 59 40	22 42 31	Hb	2	Noise
161019	18:27	300	NGC6853	19 59 40	22 42 31	Hb	2	Noise
161019	18:27	300	NGC6853	19 59 40	22 42 31	Hb	2	Noise
161019	18:45	2	NA	NA	NA	Th	2	N working
161019	18:45	2	NA	NA	NA	Th	2	N working
161019	18:45	2	NA	NA	NA	Th	2	N working
161019	18:45	2	NA	NA	NA	Th	2	N working
161019	18:58	2	NA	NA	NA	Th	2	Th cal
161019	19:10	2	Rm Star	NA	NA	Hb	2	spec.check
161019	19:10	2	Rm Star	NA	NA	Hb	2	spec.check
161019	19:10	2	Rm Star	NA	NA	Hb	2	spec.check
161019	19:47	600	NGC6853	19 59 23	22 41 16	Hb	1x100	Hb
161019	19:47	600	NGC6853	19 59 23	22 41 16	Hb	1x100	Hb
161019	19:47	600	NGC6853	19 59 23	22 41 16	Hb	1x100	Hb Fnl
161019	20:28	1	NA	NA	NA	Hb	1x100	Th cal

 doi:10.20944/preprints202209.0070.v1

Date	S.time	Exp.	Object	Ra	Dec	F.	Bin	Comments
161019	20:28	1	NA	NA	NA	Hb	1x100	Th cal
161019	20:28	1	NA	NA	NA	Hb	1x100	Th cal
161019	20:28	1	NA	NA	NA	Hb	1x100	Th cal
161019	20:28	1	NA	NA	NA	Hb	1x100	Th cal
161019	20:32	1	NA	NA	NA	Hb	1x100	W cal.
161019	20:32	1	NA	NA	NA	Hb	1x100	W cal.
161019	20:32	1	NA	NA	NA	Hb	1x100	W cal.
161019	20:32	1	NA	NA	NA	Hb	1x100	W cal.
161019	20:32	1	NA	NA	NA	Hb	1x100	W cal.
161019	20:32	1	NA	NA	NA	Hb	1x100	W cal.
161019	20:32	1	NA	NA	NA	Hb	1x100	W cal.
161019	20:35	0	NA	NA	NA	Hb	1x100	Bias Hb
161019	20:35	0	NA	NA	NA	Hb	1x100	Bias Hb
161019	20:35	0	NA	NA	NA	Hb	1x100	Bias Hb
161019	20:35	0	NA	NA	NA	Hb	1x100	Bias Hb
161019	20:39	1	NA	NA	NA	Ha	1x100	Th cal
161019	20:39	1	NA	NA	NA	Ha	1x100	Th cal
161019	20:39	1	NA	NA	NA	Ha	1x100	Th cal
161019	20:41	1	NA	NA	NA	Ha	1x100	W cal
161019	20:41	1	NA	NA	NA	Ha	1x100	W cal
161019	20:41	1	NA	NA	NA	Ha	1x100	W cal
161019	21:00	600	NGC6853	19 59 23	22 41 16	Ha	1x100	Ha Fnl

Table A.1: Observational Logs for 152 cm telescope, W - tungsten and Th - thorium

 doi:10.20944/preprints202209.0070.v1

Appendix B Python Scripts

Python script to calculate the contour plot Figure 8.3

```python
"""
Created on Sat Mar 28 16:02:23 2020

@author: robert
"""
from astropy.io import fits
from astropy.visualization import astropy_mpl_style
import matplotlib.pyplot as plt

#------------------------------------------------------------------------------
def plot(density):
    """function for plotting"""

    plt.style.use(astropy_mpl_style)
    #defining the contour plot
    plt.figure()
    plt.imshow(density, cmap= 'hot', vmin = 0 , vmax = 6500)
    plt.colorbar() #colour bar
    plt.contour(density)
    plt.grid(color='w', linestyle='-', linewidth=0.5) #grid
    plt.title('Contour plot of NGC 6853') #title
    plt.show()

def calculation(image,Header,R):
    """function that execute the calculations"""

    image_flip = image[:,::-1]

    region = image_flip[1300:2700, 200:1800]

    density = (1.8e21* region) / R

    density[density < 0] = 0
    return density

#------------------------------------------------------------------------------
#inputs and directory of the files
R = 1.3623e18
image = fits.getdata(r'/Users/robert/VB/Distro Astro shared/data/La_palma/NGC_6853_Dumbbell/Equvilent_colum_density/Av_r.fits',0)
Header = fits.getheader(r'/Users/robert/VB/Distro Astro shared/data/La_palma/NGC_6853_Dumbbell/Equvilent_colum_density/Av_r.fits',0)


"""main"""
density = calculation(image,Header,R)
plot(density)

```

Figure B.1: Python script for contour map

Python script to calculate Table 8.1

```
"""
Created on Sun Mar 29 00:05:25 2020

@author: robert
"""
import numpy as np

A0 = 6.657516                    # Initial value of Av_reduced


A_r = np.arange(A0 -0.1, A0 + 0.1 ,0.0001) #assumed range (0.31)
N_array = []                    #list of equivalent H colum density
Density = []                    # equivalent H colum density / radius of nebula


for i in range(len(A_r)):
    """loop for N and Density"""
    N = 1.8e21 * A_r[i]
    N_array.append(N)
    Den = N_array[i] / 1.3623e18
    Density.append(Den)


Std = np.std(Density)
moe = 3*Std
Mean = np.mean(Density)

print(Mean) #mean
print(moe) #margin of error
```

Figure B.2: Python script to calculate table for density